

Novel cosmological tests from combining galaxy lensing and the polarized Sunyaev-Zel'dovich effect

Oliver H. E. Philcox^{1,2,3,4,*} and Matthew C. Johnson^{5,6,†}

¹*Department of Astrophysical Sciences, Princeton University, Princeton, New Jersey 08540, USA*

²*School of Natural Sciences, Institute for Advanced Study,*

1 Einstein Drive, Princeton, New Jersey 08540, USA

³*Center for Theoretical Physics, Department of Physics, Columbia University,
New York, New York 10027, USA*

⁴*Simons Society of Fellows, Simons Foundation, New York, New York 10010, USA*

⁵*Perimeter Institute for Theoretical Physics, 31 Caroline Street North, Waterloo ON N2L 2Y5, Canada*

⁶*Department of Physics and Astronomy, York University, Toronto ON M3J 1P3, Canada*



(Received 24 June 2022; accepted 19 September 2022; published 3 October 2022)

The polarized Sunyaev-Zel'dovich (pSZ) effect is sourced by the Thomson scattering of cosmic microwave background (CMB) photons from distant free electrons and yields a novel view of the CMB quadrupole throughout the observable Universe. Galaxy shear measures the shape distortions of galaxies, probing both their local environment and the intervening matter distribution. Both observables have been shown to give interesting constraints on the cosmological model; in this work we ask: what can be learnt from their combination? The pSZ-shear cross-spectrum measures the shear-galaxy-polarization bispectrum [i.e., $\langle \gamma \delta_g(Q \pm iU) \rangle$] and contains contributions from three main phenomena: (1) the Sachs-Wolfe (SW) effect, (2) the integrated Sachs-Wolfe (ISW) effect, and (3) inflationary gravitational waves. Since the modes contributing to the pSZ signal are not restricted to the Earth's past light cone, the low-redshift cross-spectra could provide a novel constraint on dark energy properties via the ISW effect, whilst the SW signal is sourced by a coupling of scalar modes at very different times (recombination and the lensing redshift), but at similar positions; this provides a unique probe of the Universe's homogeneous time evolution. We give expressions for all major contributions to the galaxy shear, galaxy density, and pSZ auto- and cross-spectra, and evaluate their detectability via Fisher forecasts. Despite significant theoretical utility, the shear cross-spectra will be challenging to detect: combining CMB-S4 with the Rubin observatory yields a 1.6σ detection of the ISW contribution, though this increases to 5.2σ for a futuristic experiment involving CMB-HD and a higher galaxy sample density. For parity-even (parity-odd) tensors, we predict a 1σ limit of $\sigma(r) = 0.9$ (0.2) for CMB-S4 and Rubin, or 0.3 (0.06) for the more futuristic setup. Whilst this is significantly better than the constraints from galaxy shear alone (and contains fewer systematics than most auto-spectra), it is unlikely to be competitive, but may serve as a useful cross-check.

DOI: [10.1103/PhysRevD.106.083501](https://doi.org/10.1103/PhysRevD.106.083501)

I. INTRODUCTION AND MOTIVATION

Cosmology exists on the light cone. Almost all cosmological observables follow the paths of photon geodesics from their source to us, whether they be from distant galaxies or the cosmic microwave background; as such, our knowledge of the Universe is restricted to sections of the light cone. With conventional measurements, our knowledge is limited to the surface of the light cone, rather than its interior. One consequence of this is that standard cosmological observables cannot directly test cosmological homogeneity; rather, they can probe only anisotropies and time evolution, e.g., [1].

The kinetic and polarized Sunyaev-Zel'dovich (SZ) effects are different in this respect. Both are caused by the scattering of cosmic microwave background (CMB) photons from a galaxy at some radial comoving distance χ_e from the observer. Importantly, this CMB is not the same as the one observed by us today. Instead, the galaxy scatters the locally observed CMB, which is sourced by the *interior* of our past light cone as depicted in Fig. 1. If the local CMB is anisotropic, we will observe a signature from the direction of the galaxy. For the kinetic SZ (kSZ) effect, e.g., [2–8], this is caused by the CMB dipole observed by the galaxy, whose dominant component of the dipole is the galaxy's peculiar velocity. For the polarized SZ (pSZ) effect, e.g., [4,9–26], this is instead a consequence of Thomson scattering caused by the local CMB quadrupole.

*ohep2@cantab.ac.uk

†mjohnson@perimeterinstitute.ca

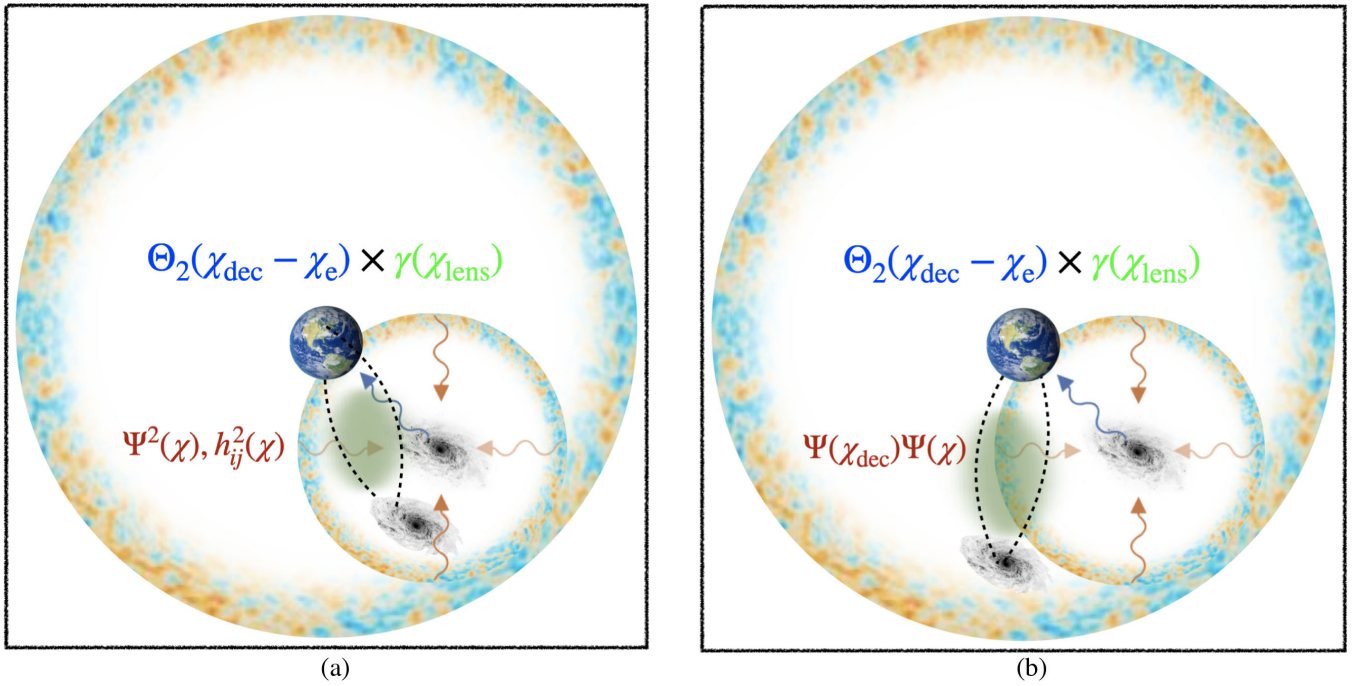


FIG. 1. (a) Tensors and the Integrated Sachs-Wolfe effect and (b) Unequal Time Sachs-Wolfe effect. Cartoon of the pSZ-shear cross-correlations considered in this work. The pSZ effect is sourced by the CMB observed at some distant galaxy (brown arrows), whose quadrupole moment, Θ_2 , is anisotropically scattered (blue arrow) and reaches the Earth. This is sensitive to physics on the light cone of the distant galaxy, and that between the distant galaxy and the Earth. In contrast, shear is sourced by the perturbations to a photon geodesic imprinted by scalars, Ψ , and tensors, h_{ij} , as it traverses its worldline on the Earth’s light cone (shown in black dotted lines). If the lens (green region) lies close to the scattering galaxy, a correlation will be induced due to both sets of photons (scattered CMB and weak lensing) experiencing the same scalar (through the integrated Sachs-Wolfe effect) and tensor modes. If the lens lies further than the pSZ source, other correlations can arise, such as one between the scalar potential at last scattering, $\Psi(\chi_{\text{dec}})$ and that sourcing gravitational lensing. Unlike most physics observables, this correlates two effects at very different times but at the same physical location.

Such effects propagate to a distortion in the CMB temperature and polarization anisotropies measured on Earth that correlate with the galaxy density at the scattering location; by utilizing this correlation, one can extract the dipole and quadrupole *fields* as a function of position and distance, e.g., [7,8,10,12,16,19]. Crucially, this is a measurement of two things: (a) the CMB primaries and secondaries observed at the source at χ_e (orange arrow in Fig. 1) and (b) the distribution of matter between χ_e to the observer at $\chi = 0$ (blue arrow in Fig. 1). Only the latter quantity is constrained to lie *on* the Earth’s light cone; the former lies instead *within* it, as a result of photons taking a nondirect route to the Earth, and is the subject of interest in this work.

Cosmic shear is a key observable in 21st century cosmology. This measures the shape distortions of galaxies as a function of position and distance, which carries information both about the galaxies’ local environments (via the “intrinsic alignment” mechanism, e.g., [27]), and the intervening spacetime (via gravitational lensing, e.g., [28]). In contrast to kSZ and pSZ these quantities lie on the light cone (or at least on its first-order perturbations); however, they are sensitive to a number of interesting features. Conventionally, cosmic shear is used to probe the

integrated matter density from a source at some distance χ_{lens} from the observer (located at $\chi = 0$), and has been shown to give tight constraints on the matter density and clustering amplitude, e.g., [29]. Noting that the matter density is nothing but a gauge transform of the scalar metric potential, one may ask whether galaxy shapes are sensitive to other metric perturbations, such as gravitational waves. As shown in a number of works e.g., [30–33], such an effect does exist, and contributes both to lensing and intrinsic alignment. This occurs since the galaxy shape is a tensorial (spin-two) observable, and thus can couple to tensor metric perturbations. Unfortunately, the size of such an effect is generally small, since gravitational waves significantly decay after inflation, and, moreover, the principal observable, the shear *B* mode, is usually discarded on the grounds of systematics or just used for null tests, e.g., [29]. As such, most efforts to measure gravitational waves have been directed towards the primary CMB.

The next decade will yield unprecedented volumes of cosmological data, both from the CMB, due to experiments such as the Simons Observatory [34] and CMB-S4 [35], and large-scale structure (LSS), with photometric surveys such as Rubin (hereafter VRO) [36] and Euclid, as well as

spectroscopic instruments including DESI [37] and MegaMapper [38]. The incoming avalanche motivates us to consider new ways of probing the Universe, in particular those constraining hitherto poorly understood degrees of freedom. In this work, we will add to such an effort by considering the detectability and utility of cross-correlations between the pSZ contribution to the CMB polarization anisotropies and cosmic shear [i.e., a $\langle \gamma g(Q \pm iU) \rangle$ three-point function]. The physical consequences of each observable have been considered in the past, e.g., [11,18,24,25,28,29,32,39], however the correlations described in Fig. 1 have yet to be assessed. Performing analyses using cross-spectra can be particularly enlightening since (a) they are often less sensitive to systematic effects than auto-spectra, and (b) incomplete correlations can allow specific, and interesting, pieces of the signal to be extracted. That said, a strong correlation is needed for an observable to be useful, and it is unclear, *a priori*, whether pSZ and shear (or indeed, pSZ and galaxy positions) satisfy this.

There are two sources of scalar pSZ-shear correlations. The first occurs when the observables probe matter in the same region of space at similar times, as in Fig. 1(a). An important contributor to the pSZ signal is the integrated Sachs-Wolfe (ISW) effect, e.g., [23,24], which probes the Universe in the vicinity of the scattering galaxy at χ_e ; for shear, photons emanating from the galaxy at $\chi_{\text{lens}} \gtrsim \chi_e$ are lensed by the same matter distribution.¹ In this way, the pSZ-shear correlation probes the local potential (or rather its time derivative), via the ISW effect, and, unlike detections obtained from the primary CMB is not limited to the Earth's light cone.

The second possibility is to have correlations between spatially close regions of the Universe at vastly different times. This principally occurs for $\chi_{\text{lens}} > \chi_e$, whence the gravitational potential sourcing lensing (at a time $\chi < \chi_e$) is also the source of Sachs-Wolfe (SW) effects at the local last-scattering surface seen (after rescattering) in the pSZ effect. Since pSZ is not restricted to the light cone, this scenario is fully permissible [cf. Fig. 1(b)] and arises since the scattering photon does not take a direct path from the redshift of decoupling until today. Mathematically, the phenomena is caused by a correlation of the SW potential $\Psi(\mathbf{x}, \chi_{\text{dec}})$ and the lensing potential $\Psi(\mathbf{x}', \chi)$ at large relative time ($\chi \ll \chi_{\text{dec}}$) but small relative position ($|\mathbf{x} - \mathbf{x}'| \ll \chi$). The ability to correlate potentials at such different times is particularly unusual in cosmology (and made possible only via the off-light-cone effects), and its detection would certainly be of great interest. If measured, this would allow one to probe the local growth function $D(\chi, \mathbf{x})$ at two redshifts simultaneously, and, in principle, allow for a

¹Strictly, such a correlation can be sourced also by the lensing of pSZ photons after their scattering; this phenomena is second order however, and likely to be small.

spatially resolved map of $D(\chi, \mathbf{x})/D(\chi_{\text{dec}}, \mathbf{x})$, given additional geometric information (cf. Sec. VI).

Gravitational waves can also be probed using the cross-correlation of pSZ and shear. The intuition for this is straightforward: both pSZ and shear measure tensorial quantities, the CMB quadrupole and the galaxy shape tensor γ_{ij} . For pSZ, tensor signatures (of both odd and even parity) arise in the same manner as the primary CMB: predominantly from the gravitational effects imparted on radiation in the time after recombination, whilst for shear, this is sourced by lensing and intrinsic effects. While gravitational wave signatures in shear are very weak [30–33], they have been shown to be observable in the pSZ signal accessible to future experiments [10,11,15], thus it is interesting to consider whether their cross-correlation can be of use, and whether the pSZ can be used to boost the small tensorial signal present within LSS probes. Unlike for scalars, the measurement of tensors in the primary CMB is not cosmic-variance limited (since the *B*-mode signal is, under null linear assumptions, zero), though pSZ can still add information by increasing the number of fundamental modes available. As described above, cross-correlations could be of use in making such a detection, since they do not suffer from many of the traditional systematic effects such as atmospheric dust absorption (since they contain only one power of the CMB), thus it is important to explore whether such statistics can be practically useful.

In the remainder of this work, we consider whether future surveys are capable of measuring the pSZ-shear cross-correlation. Such a detection could place further constraints on novel observables, be it stronger bounds on the ISW effect, the strongly unequal-time SW effect, or tensor modes. After laying out our conventions in Sec. II, we will present the contributions to galaxy shear, galaxy density, and the pSZ effect from scalars and tensors in Sec. III and from noise in Sec. IV. Our main results are forecasts on the detectability of the cross-spectra themselves and various physical components, which we present in Sec. V. In Sec. VI we describe the novel properties illustrated in Fig. 1 in the context of a toy model before concluding in Sec. VII. Appendix A lists the transfer functions used in this work, whilst Appendix B presents a brief forecast of the kSZ autocorrelation and cross-correlation. All calculations are made publicly available.²

II. CONVENTIONS

We briefly present the various conventions for scalar and tensor perturbations used in this work, as well as for cosmic shear. Note that conventions differ between works, e.g., our results appear to differ from those of [12,32] until notational variations are taken into account.

²<https://GitHub.com/OliverPhilcox/pSZ-cross-Shear>.

A. Scalar modes

We primarily work with the Newtonian potential, Ψ , which enters the Friedman-Robertson-Lemaître-Walker metric in the standard fashion (in the conformal Newtonian gauge, with $c = 1$):

$$ds^2 = a^2(\eta)[-(1 + 2\Psi)d\eta^2 + (1 - 2\Psi)dx^i dx_i], \quad (1)$$

assuming the stress-free condition. The statistics of Ψ are described by its power spectrum:

$$\langle \Psi(\mathbf{k}, \chi) \Psi^*(\mathbf{k}', \chi') \rangle = (2\pi)^3 \delta_{\mathbb{D}}(\mathbf{k} - \mathbf{k}') P_{\Psi}(k, \chi, \chi'), \quad (2)$$

where P_{Ψ} can be written in terms of the dimensionless spectrum \mathcal{P}_{Ψ} via $P_{\Psi}(k, \chi, \chi') = D_{\Psi}(\eta_0 - \chi) D_{\Psi}(\eta_0 - \chi') (2\pi^2/k^3) \mathcal{P}_{\Psi}(k)$, where D_{Ψ} is the potential growth function, η_0 is the conformal time today, and we absorb the necessary transfer functions into $\mathcal{P}_{\Psi}(k)$. Explicit forms for the potential growth function (on super- and subhorizon scales) can be found in [2,40], and we note that $D_{\Psi}(a) \rightarrow (9/10)D_+(a)/a$ in the subhorizon limit, for the usual growth function $D_+(a)$. Practically, P_{Ψ} can be obtained from the matter power spectrum computed by CLASS, rescaling by the ratio of potential and density growth factors.

We will also require the velocity power spectra. On sufficiently large scales, this is given by [40]

$$\mathbf{v}(\mathbf{r}, \chi) = -D_v(\chi)/D_{\Psi}(\chi) \nabla \Psi(\mathbf{k}, \chi) \quad (3)$$

utilizing the velocity growth factor

$$D_v(\chi) = \frac{2a^2 H(a)}{H_0^2 \Omega_m} \frac{y(\chi)}{4 + 3y(\chi)} \left[D_{\Psi}(\chi) + \frac{dD_{\Psi}(\chi)}{d \log a} \right], \quad (4)$$

where $y(\chi) = a(\chi)/a_{\text{eq}}$.

B. Tensor modes

We define the transverse-traceless tensor metric perturbation, h_{ij} , via

$$ds^2 = a^2(\eta)[-d\eta^2 + (\delta_{ij}^{\mathbf{k}} + h_{ij})dx^i dx^j]. \quad (5)$$

This is often written in terms of $+$, \times states via

$$h_{ij}(\mathbf{r}, \eta) = \tilde{h}_+(\mathbf{r}, \eta) e_{ij}^+(\hat{\mathbf{r}}) + \tilde{h}_\times(\mathbf{r}, \eta) e_{ij}^\times(\hat{\mathbf{r}}). \quad (6)$$

In this work, we primarily expand in helicity states:

$$h_{ij}(\mathbf{r}, \chi) = \int_{\mathbf{k}} e^{i\mathbf{k}\cdot\mathbf{r}} \sum_{\lambda \in \pm} h_{\lambda}(\mathbf{k}, \chi) e_{ij}^{(\lambda)}(\hat{\mathbf{k}}), \quad (7)$$

where $e_{ij}^{(\lambda)} e_{(-\lambda)}^{ij} = 1$, $h_{\lambda} = e_{(-\lambda)}^{ij} h_{ij}$, and we notate $\int_{\mathbf{k}} \equiv \int d\mathbf{k}/(2\pi)^3$. Here, $e_{ij}^{(\lambda)} = e_i^{(\lambda)} e_j^{(\lambda)}$ with $\mathbf{e}^{(\lambda)} = (\mathbf{e}_1 \mp i\lambda \mathbf{e}_2)/\sqrt{2}$

where $\{\hat{\mathbf{k}}, \mathbf{e}_1, \mathbf{e}_2\}$ form an orthonormal set. These are related to the $\tilde{h}_{+, \times}$ basis by $h_{\pm} = (\tilde{h}_+ \mp i\tilde{h}_{\times})/2$.

The statistics of h are specified by

$$\langle h_{\lambda}(\mathbf{k}, \chi) h_{\lambda'}^*(\mathbf{k}', \chi') \rangle = (2\pi)^3 \delta_{\mathbb{D}}(\mathbf{k} - \mathbf{k}') P_{h_{\lambda}}(k, \chi, \chi'), \quad (8)$$

with the total power spectrum $P_h = [P_{h_+} + P_{h_-}]$, and chiral spectrum $\Delta_h P_h = [P_{h_+} - P_{h_-}]$.³ This is related to the primordial spectrum $\mathcal{P}_h(k)$ via

$$P_h(k, \chi, \chi') = \frac{2\pi^2}{k^3} D_{\text{T}}(k, \eta_0 - \chi) D_{\text{T}}(k, \eta_0 - \chi') \mathcal{P}_h(k), \quad (9)$$

where $D_{\text{T}}(k, \eta) \approx 3j_1(k\eta)/(k\eta)$ is the tensor transfer function, assuming matter domination. The tensor spectrum is usually parametrized as

$$\mathcal{P}_h(k) = \Delta_{\text{T}}^2 \left(\frac{k}{k_*} \right)^{n_{\text{T}}}, \quad (10)$$

where $n_{\text{T}} \approx -r/8$ is the spectral index and $\Delta_{\text{T}}^2 = r\Delta_{\zeta}^2$ is the amplitude, for curvature perturbation ζ , and characteristic scale k_0 .

C. Shear

We define the components of the full-sky shear as ${}_{\pm 2}\gamma(\hat{\mathbf{n}}) = m_{\mp}^i m_{\mp}^j \gamma_{ij}(\hat{\mathbf{n}})$, where the basis vectors are

$$\mathbf{m}_{\pm} = \frac{1}{\sqrt{2}} \begin{pmatrix} \cos \theta \cos \varphi \pm i \sin \varphi \\ \cos \theta \sin \varphi \mp i \cos \varphi \\ -\sin \theta \end{pmatrix}. \quad (11)$$

The spherical harmonic coefficients are defined via

$$\begin{aligned} {}_{+2}\gamma_{\ell m} &= \sqrt{\frac{(\ell-2)!}{(\ell+2)!}} \int d\hat{\mathbf{n}} Y_{\ell m}^*(\hat{\mathbf{n}}) \bar{\delta}^2 {}_{+2}\gamma(\hat{\mathbf{n}}), \\ {}_{-2}\gamma_{\ell m} &= \sqrt{\frac{(\ell-2)!}{(\ell+2)!}} \int d\hat{\mathbf{n}} Y_{\ell m}^*(\hat{\mathbf{n}}) \delta^2 {}_{-2}\gamma(\hat{\mathbf{n}}), \end{aligned} \quad (12)$$

where δ and $\bar{\delta}$ are the usual spin-raising and spin-lowering operators, e.g., [41]. These are related to the E and B modes via ${}_{\pm 2}\gamma_{\ell m} = \gamma_{\ell m}^E \pm i\gamma_{\ell m}^B$. The corresponding power spectra are

$$C_{\ell}^{\gamma^X \gamma^Y} = \frac{1}{2\ell+1} \sum_{m=-\ell}^{\ell} \langle \gamma_{\ell m}^X \gamma_{\ell m}^{Y*} \rangle, \quad (13)$$

for $X \in \{E, B\}$, which is parity even (odd) if $X = Y$ ($X \neq Y$).

³In the notation of [11], $P_{h_+} = P_L/2$, $P_{h_-} = P_R/2$, $\Delta_c = -\Delta_h$ and $P_h^{\text{this work}} = P_h^{\text{former}}/2$.

III. SIGNAL MODELING

In this section, we describe how to compute the signal auto- and cross-spectra for galaxy density, galaxy shear, and the remote quadrupole field, considering both scalar and tensor sources.

A. Galaxy density

The basic observable in a galaxy redshift survey is the galaxy overdensity. The overdensity in a shell at fixed comoving radial distance is $\delta_g(\chi\hat{\mathbf{n}}) = [n(\chi\hat{\mathbf{n}}) - n(\chi)]/n(\chi)$, for observed field $n(\chi\hat{\mathbf{n}})$, and depends principally on the scalar potential Ψ . At linear order, we have the usual relation,

$$\begin{aligned}\delta_g(\chi\hat{\mathbf{n}}) &= b_g(\chi) \int_{\mathbf{k}} e^{ik\chi\hat{\mathbf{n}}} \delta_m(\mathbf{k}, \chi) \\ &= -\frac{2a(\chi)}{3H_0^2\Omega_m} b_g(\chi) \int_{\mathbf{k}} e^{ik\chi\hat{\mathbf{n}}} k^2 \Psi(\mathbf{k}, \chi),\end{aligned}\quad (14)$$

where $\delta_m(\mathbf{k}, \chi)$ is the Fourier-space matter density, related to Ψ via the Poisson equation, and we neglect relativistic effects. In this paper, we will consider photometric galaxy surveys where the galaxy density is measured in redshift bins labeled $a = 1, 2, \dots, N_{\text{bin}}$ and given by

$$\delta_{g,a}(\hat{\mathbf{n}}) = \int_0^\infty d\chi n_a(\chi) \delta_g(\chi\hat{\mathbf{n}}),\quad (15)$$

where $n_a(\chi) \propto n(\chi)W_a(\chi)$ is the normalized source density in bin a , as before.⁴ This uses the true source density $n(\chi)$ and a user-defined weighting function $W_a(\chi)$. Note that here and everywhere below we neglect redshift space distortions, magnification, and relativistic projection effects. There are only scalar contributions to this observable.

$$\begin{aligned}\pm 2\gamma_{\text{T},a}(\hat{\mathbf{n}}) &= \int_0^\infty d\chi n_a(\chi) \left[-\frac{1}{2} h_{\pm}(\mathbf{0}, 0) - \frac{1}{2} [1 - b_{\text{T}}(\chi)a^{-2}(\chi)(\partial_\eta^2 + aH\partial_\eta)] h_{\pm}(\chi\hat{\mathbf{n}}, \chi) \right. \\ &\quad \left. - \int_0^\chi d\chi' \left[\frac{\chi - \chi'}{2} \frac{\chi'}{2\chi} m_{\mp}^i m_{\mp}^j h_{kl,ij} \hat{\mathbf{n}}^k \hat{\mathbf{n}}^l + \left(1 - \frac{2\chi'}{\chi} \right) \hat{\mathbf{n}}^l m_{\mp}^k m_{\mp}^i h_{kl,i} - \frac{1}{\chi} h_{\pm}(\chi'\hat{\mathbf{n}}, \chi') \right] \right]\end{aligned}\quad (18)$$

for $h_{\pm} \equiv m_{\mp}^i m_{\mp}^j h_{ij}$, where our tensor conventions are specified in Sec. II B. The first and second terms on the first line correspond to observer and source distortions (frame of reference effects), the third term is from intrinsic alignments, and the second line gives contributions

⁴In the limit of $N_{\text{bin}} \rightarrow \infty$ this is analogous to a three-dimensional spectroscopic sample, except without redshift effects.

B. Galaxy shear

The shape distortions of galaxies are usually expressed using the shear tensor γ_{ij} (neglecting higher-order moments such as flexion, e.g., [42]). Roughly speaking, this is a measurement of a galaxy's ellipticity, and is usually projected onto the two-sphere by binning in redshift, i.e.,

$$\gamma_{ij,a}(\hat{\mathbf{n}}) = \int_0^\infty d\chi n_a(\chi) \gamma_{ij}(\chi\hat{\mathbf{n}}),\quad (16)$$

where $\chi\hat{\mathbf{n}}$ is the three-dimensional galaxy position at comoving distance χ , and $n_a(\chi) \propto n(\chi)W_a(\chi)$ is the normalized source density in bin a , for source density $n(\chi)$, as before. Following projection, the shear tensor is a spin-two field and can be expressed in $\pm 2\gamma$ components or E and B modes (cf. Sec. II C).

The Newtonian potential Ψ sources two contributions to galaxy shear: intrinsic alignments and weak lensing. For a source galaxy at redshift χ , the spin- ± 2 shear components are given by, e.g., [27,28,41,43]:

$$\begin{aligned}\pm 2\gamma_{\text{S},a}(\hat{\mathbf{n}}) &= \int_0^\infty d\chi n_a(\chi) \left[-b_{\text{S}}(\chi) m_{\mp}^i m_{\mp}^j \Psi_{,ij}(\chi\hat{\mathbf{n}}, \chi) \right. \\ &\quad \left. + 2 \int_0^\chi d\chi' \frac{\chi - \chi'}{\chi'} m_{\mp}^i m_{\mp}^j \Psi_{,ij}(\chi'\hat{\mathbf{n}}, \chi') \right],\end{aligned}\quad (17)$$

where m_{\pm} are the basis components given in Sec. II C. The first term is the intrinsic alignment contribution (arising from galaxies preferentially aligning with a local tidal field), and involves the intrinsic alignment bias $b_{\text{S}}(\chi) \equiv (2/3)C_1^{\text{S}}\rho_{c,r0}H_0^{-2}$ (in the notation of [32,44]), with $\rho_{c,r0} = 3H_0^2/(8\pi G)$, and $C_1^{\text{S}}\rho_{c,r0} \sim 0.1$. The second term is from weak lensing, and involves the integrated scalar perturbation along the photon's worldline from the source galaxy to the observer.

Following [32], tensor modes source the following contributions to galaxy shear:

integrated along the line of sight from the source to the observer, i.e., weak lensing effects. The coefficient $b_{\text{T}}(\chi) \equiv (2/3)C_1^{\text{T}}\rho_{c,r0}H_0^{-2}$ specifies the strength of the alignment effect with $C_1^{\text{T}} \sim C_1^{\text{S}}$ expected in practice (though see [31,33] for further discussion of this).

C. Remote quadrupole

The polarized Sunyaev Zel'dovich (pSZ) effect sources polarization anisotropies through the Thomson scattering

of CMB photons from the locally observed CMB quadrupole seen by free electrons in the post-reionization Universe (the remote quadrupole field). Given a tracer of the optical depth, such as a galaxy redshift survey, and high-resolution measurements of the CMB polarization, it is possible to reconstruct the remote quadrupole field using a quadratic estimator as described in [10,11,15]. In essence, this estimator probes the combination $\delta_{g,a}(Q \pm iU)$, thus its auto-spectra is really a four-point function of the form $\langle \delta_{g,a}^2(Q \pm iU)^2 \rangle$. The remote quadrupole field at some position $\chi \hat{n}$ is defined by

$$\Theta_{2m}(\chi \hat{n}) = \int d\hat{n}' \Theta(\chi \hat{n}, \hat{n}') Y_{2m}^*(\hat{n}'), \quad (19)$$

where \hat{n}' is the emission angle and Θ is the temperature perturbation. There are contributions to Θ_{2m} from both scalar and tensor modes via the usual Sachs-Wolfe, integrated Sachs-Wolfe, and Doppler components. The quantity reconstructed in pSZ tomography is a projection of the remote quadrupole field onto our line of sight, and integrated over radial bins with the same weighting as the galaxy density:

$$q_a^\pm(\hat{n}) = \int_0^\infty d\chi n_a(\chi) \sum_{m=-2}^2 \Theta_{2m}(\chi \hat{n})_{\mp 2} Y_{2m}(\hat{n}), \quad (20)$$

where $_{\mp 2} Y_{2m}(\hat{n})$ are spin-weighted spherical harmonic. As for shear, we can form E and B modes in harmonic space as $q_{\ell m,a}^\pm = q_{\ell m,a}^E \pm i q_{\ell m,a}^B$. Scalar perturbations source only an E mode, while tensors source both E and B modes.

D. Spectra

Having defined each of the observables above, can write a general element of the signal covariance in terms of an integral of transfer functions convolved with primordial spectra. For scalars, we have

$$C_{\ell,ab}^{XY}|_S = 4\pi \int_0^\infty d \log k \Delta_{\ell,a}^{X,S}(k,\chi) \Delta_{\ell,b}^{Y,S*}(k,\chi') \mathcal{P}_\Psi(k), \quad (21)$$

where $X, Y \in \{\delta_g, \gamma^E, q^E\}$. The explicit form of the transfer functions $\Delta_{\ell,a}^{X,S}(k,\chi)$ is presented in Appendix A. For tensors, we find a similar form:

$$C_{\ell,ab}^{XY}|_T = 4\pi \int_0^\infty d \log k \Delta_{\ell,a}^{X,T}(k,\chi) \Delta_{\ell,b}^{Y,T*}(k,\chi') \mathcal{P}_h(k) \times [\delta_K^{XY} + (1 - \delta_K^{XY}) \Delta_h], \quad (22)$$

where δ_K^{XY} is the Kronecker delta, the last term encodes chirality, $X, Y \in \{\gamma^E, q^E, \gamma^B, q^B\}$, and we assume $\ell \geq 2$. The explicit form of the tensor transfer functions $\Delta_{\ell,a}^{X,T}(k,\chi)$ is again given in Appendix A.

IV. NOISE MODELING

For the forecasts presented below, we must make some assumptions about the hypothetical galaxy survey and CMB experiment used to measure the galaxy density, shear, and remote quadrupole field. The galaxy density and shear are limited by the mean number density of objects in the survey, \bar{n} ; for the galaxy density, this sources noise spectra of the form

$$C_{\ell,ab}^{\delta_g \delta_g}|_{\text{noise}} = \frac{1}{\bar{n}_a} \delta_{ab}^K, \quad (23)$$

where $\bar{n}_a^{-1} = \int_0^\infty d\chi n(\chi) W_a^2(\chi) / [\int_0^\infty d\chi n(\chi) W_a(\chi)]^2$. For shear, the noise spectra are given by

$$C_{\ell,ab}^{X\gamma Y}|_{\text{noise}} = \frac{\sigma_\gamma^2}{\bar{n}_a} \delta_{ab}^K \delta_K^{XY}, \quad (24)$$

with $X, Y \in \{E, B\}$.

The noise on the reconstructed remote quadrupole field is somewhat more complex, as it is dependent on the estimator, galaxy survey, CMB experiment, and signal spectra. The quadratic estimator for the remote dipole of the form

$$\hat{q}_{\ell m,a}^X = \sum_{\ell_1 m_1 \ell_2 m_2} (W_{\ell m \ell_1 m_1 \ell_2 m_2}^{X,E} a_{\ell_1 m_1}^E + W_{\ell m \ell_1 m_1 \ell_2 m_2}^{X,B} a_{\ell_1 m_1}^B) \Delta \tau_{\ell_2 m_2, a}, \quad (25)$$

for $X \in \{E, B\}$ (using the decomposition of Sec. II C), where $a_{\ell m}^{E,B}$ are the CMB E and B modes, $\Delta \tau_a$ is the optical depth in bin a , and W are some weight matrices whose form can be found in [10]. From [12], the estimator noise is given by

$$\frac{1}{C_{\ell,ab}^{q^E q^E}|_{\text{noise}}} = \frac{\delta_K^{ab}}{2\ell+1} \sum_{\ell_1 \ell_2} \frac{\Gamma_{\ell \ell_1 \ell_2, a}^{\text{pSZ}} \Gamma_{\ell \ell_1 \ell_2, b}^{\text{pSZ}}}{(|\alpha_{\ell \ell_1 \ell_2}|^2 C_{\ell_1}^{EE} + |\gamma_{\ell \ell_1 \ell_2}|^2 C_{\ell_1}^{BB}) C_{\ell_2, ab}^{\delta_g \delta_g}},$$

$$\frac{1}{C_{\ell,ab}^{q^B q^B}|_{\text{noise}}} = \frac{\delta_K^{ab}}{2\ell+1} \sum_{\ell_1 \ell_2} \frac{\Gamma_{\ell \ell_1 \ell_2, a}^{\text{pSZ}} \Gamma_{\ell \ell_1 \ell_2, b}^{\text{pSZ}}}{(|\gamma_{\ell \ell_1 \ell_2}|^2 C_{\ell_1}^{EE} + |\alpha_{\ell \ell_1 \ell_2}|^2 C_{\ell_1}^{BB}) C_{\ell_2, ab}^{\delta_g \delta_g}}, \quad (26)$$

with vanishing $C_{\ell,ab}^{q^E q^B}|_{\text{noise}}$ due to parity conservation. In the above, $|\alpha|^2$ ($|\gamma|^2$) is one if $\ell + \ell_1 + \ell_2$ is even (odd) and zero elsewhere, and the CMB spectra $C_\ell^{EE, BB}$ include lensing and noise. Here, the weighting function is given by

$$\Gamma_{\ell \ell_1 \ell_2, a}^{\text{pSZ}} = -\frac{\sqrt{6}}{10} \sqrt{\frac{(2\ell+1)(2\ell_1+1)(2\ell_2+1)}{4\pi}} \times \begin{pmatrix} \ell & \ell_1 & \ell_2 \\ 2 & -2 & 0 \end{pmatrix} C_{\ell_2, ab}^{\Delta \tau \delta_g}, \quad (27)$$

where the quantity in parentheses is a Wigner $3j$ symbol. The galaxy-galaxy and galaxy-optical depth spectra used in

the noise computation, assuming that ionized gas traces dark matter on all scales,⁵ are given by

$$\begin{aligned} C_{\ell,ab}^{\delta_g\delta_g} &= 4\pi \int_0^\infty d \log k \left[\int_0^\infty d\chi n_a(\chi) b_g(\chi) D_+(\eta_0 - \chi) j_\ell(k\chi) \right] \left[\int_0^\infty d\chi' n_b(\chi') b_g(\chi') D_+(\eta_0 - \chi') j_\ell(k\chi') \right] \mathcal{P}_\delta(k) + \frac{1}{\bar{n}_a} \delta_{ab}^K \\ C_{\ell,ab}^{\Delta\tau\delta_g} &= 4\pi \int d \log k \left[\int_0^\infty d\chi \sigma_T a(\chi) W_a(\chi) n_e(\chi) D_+(\eta_0 - \chi) j_\ell(k\chi) \right] \left[\int_0^\infty d\chi' n_b(\chi') b_g(\chi') D_+(\eta_0 - \chi') j_\ell(k\chi') \right] \mathcal{P}_\delta(k), \end{aligned} \quad (28)$$

where we introduce the matter power spectrum $\mathcal{P}_\delta(k) \equiv (k^3/2\pi^2)P_\delta(k, z=0)$ with growth factor D_+ , electron density $n_e(\chi)$, and the Thomson cross section σ_T . Since we require these spectra at large ℓ , they are computed with the Limber approximation (including nonlinear effects only through \mathcal{P}_δ).

V. DETECTABILITY FORECASTS

We now turn to the question of whether the above effects are measurable in practice. To ascertain this, we will consider a simple forecast appropriate for next-generation observatories, aiming to measure both the signal to noise of the various signals and the detectability of cosmological parameters such as the tensor-mode amplitude.

For these forecasts, we assume the following:

- (i) *Galaxy sample*: VRO-like (LSST gold sample), with $n(z) \propto z^2 \exp(-z/z_0)$ for $z_0 = 0.3$ with a source density of 40 arcmin^{-2} , ignoring photometric redshift errors [36]. We assume linear bias $b(z) = 0.95/D_+(z)$ for growth factor $D_+(z)$ and a sky fraction of $f_{\text{sky}} = 0.36$.⁶
- (ii) *Binning*: Six bins with $z \in [0.1, 6]$, each a top hat in comoving distance with $\Delta\chi \approx 1600 \text{ Mpc}$. The inverse galaxy density varies from 6 to $0.0002 \text{ arcmin}^{-2}$ from low to high redshift. We include all necessary cross covariances in our forecasting, and will discuss the dependence on z_{max} and the number of bins below.
- (iii) *CMB*: Gaussian instrumental noise and beam, taking the standard form $N_\ell^{E,B} = \Delta_p^2 \exp[\ell(\ell+1)\theta_{\text{FWHM}}/8 \log 2]$, for noise $\Delta_p = 1 \mu\text{K-arcmin}$ and beam width $\theta_{\text{FWHM}} = 1 \text{ arcmin}$, as appropriate for

⁵This is related to the so-called optical depth bias. Because the pSZ signal is dependent on the optical depth, and we reconstruct it with an imperfect tracer (galaxies in this case), there is modeling uncertainty implicit in the estimator that can bias the reconstructed remote quadrupole field. We do not incorporate an analysis of the optical depth degeneracy in this work.

⁶As noted in [45], a deeper sample of galaxies can be obtained from VRO by including drop-outs with a higher magnitude limit. Whilst this would aid the detectabilities considered herein, we do not include it, since the additional high-redshift galaxies will not be measured at sufficiently high resolution to enable shear measurement. Furthermore, we note that the forms of $n(z)$ and $b(z)$ are uncertain at high redshift. Since the high- z data add little constraining power (cf. Sec. V B), this is unlikely to significantly affect our forecast.

CMB-S4 [35]. We will also consider a higher resolution sample with $\Delta_p = 0.5 \mu\text{K-arcmin}$ noise, a 0.25 arcmin beam and a source density of 100 arcmin^{-2} over $f_{\text{sky}} = 0.5$, similar to CMB-HD [46].⁷

- (iv) *Cosmological parameters*: For ΛCDM : $\{h=0.7, A_s=1.95 \times 10^{-9}, n_s=0.96, \Omega_b=0.049, \Omega_m=0.3\}$. For tensors, we set $r_{\text{fid}} = 1$ for illustration, with $k_0 = 0.05 \text{ Mpc}$ and $n_t = -r/8$. Where relevant, we assume maximal chirality, i.e., $\Delta_h = 1$.

All power spectra are computed in PYTHON via explicit integration of the kernels given above against scalar and tensor power spectra, given by CLASS, using all ℓ in the range $[2, 100]$ (noting that the signal to noise falls quickly with ℓ). For the pSZ noise spectra, we compute the lensed CMB spectra up to $\ell = 10^4$ using CLASS, with the optical depth spectra computed assuming that $n_e(\chi) = (7/8)n_b(\chi)$ (appropriate for a hydrogen fraction of $3/4$), and assume full ionization with the electron inhomogeneities tracing those of matter, ignoring optical depth degeneracies. To evaluate (26) we perform a direct sum over ℓ_1, ℓ_2 for $\ell_i \in [1, 10000]$, with the relevant Wigner $3j$ symbols precomputed using recurrence relations,⁸ and the high- ℓ galaxy and optical depth spectra computed using the Limber approximation, e.g., [43]. JUPYTER notebooks containing all the analysis code (and a number of associated plots) can be found (see footnote 2).

In the Gaussian limit, the various signals (including noise contributions) have covariance:

$$\text{Cov}(C_{\ell,ab}^{XY}, C_{\ell',cd}^{ZW}) = \frac{2\delta_{\ell\ell'}^K}{(2\ell+1)f_{\text{sky}}} [C_{\ell,ac}^{XZ} C_{\ell,bd}^{YW} + C_{\ell,ad}^{XW} C_{\ell,bc}^{YZ}], \quad (29)$$

which is diagonal in ℓ . When considering the detectability of pSZ signals, only noise and scalar shear spectra appear on the rhs of (29), but when considering tensors, we include also scalar pSZ contributions as an effective noise term.

⁷Note that we neglect any leakage between temperature and polarization in the CMB experiments; this could potentially lead to a percent-level bias in the high- ℓ polarization spectra, which would have severe implications for pSZ detectability.

⁸We use the implementation of <https://github.com/xzackli/WignerFamilies.jl>.

The Fisher matrix takes the standard form, e.g., [47],

$$F_{\alpha\beta} = \sum_{\ell} \frac{d\mathbf{D}_{\ell}}{dp_{\alpha}} \mathbf{C}_{\ell}^{-1} \frac{d\mathbf{D}_{\ell}}{dp_{\beta}}, \quad (30)$$

for some set of parameters $\{p_{\alpha}\}$, where the data vector, \mathbf{D}_{ℓ} , and covariance \mathbf{C}_{ℓ} , contain all nontrivial auto- and cross-spectra. Using six tomographic bins, we find a total of 42 (156) parity-even and 36 (144) parity-odd spectra for pSZ or shear (pSZ and shear). Under null assumptions, parity-odd and parity-even spectra are uncorrelated, thus we may compute their contributions to Fisher forecasts separately. Via the Cramer-Rao bound, the 1σ bound on p_{α} satisfies $\sigma_{p_{\alpha}}^2 \geq (F^{-1})_{\alpha\alpha}$.

A. Numerical results

Figure 2 displays the auto- and cross-spectra of pSZ and galaxy shear for a single redshift bin, separating out scalar,

tensor, and noise components. As expected, the shear-shear spectra contain strong scalar contributions (which form the workhorse of many previous $S_8 - \Omega_m$ analyses), but, as in [32], only very weak contributions from tensors. Even in the B mode (which is not cosmic-variance limited), the signature of $r = 1$ gravitational waves can be orders of magnitude below the noise floor of CMB-S4/VRO, and accessible only at the smallest ℓ , where foreground and systematic effects are most important. At higher redshift, shear is of greater use, though upcoming photometric surveys are optimized only for the relatively local Universe.

For pSZ auto-spectra, the noise threshold remains a significant limitation, but, as seen in the middle panel of Fig. 2, both scalars and tensors can be potentially detected on very large scales, matching the results of previous work, e.g., [10,12]. In contrast to the shear autocorrelation, the tensor spectra is relatively evenly split between E and B modes; this occurs since the scalar E -mode contribution is weak, thus the pSZ noise limits both samples.

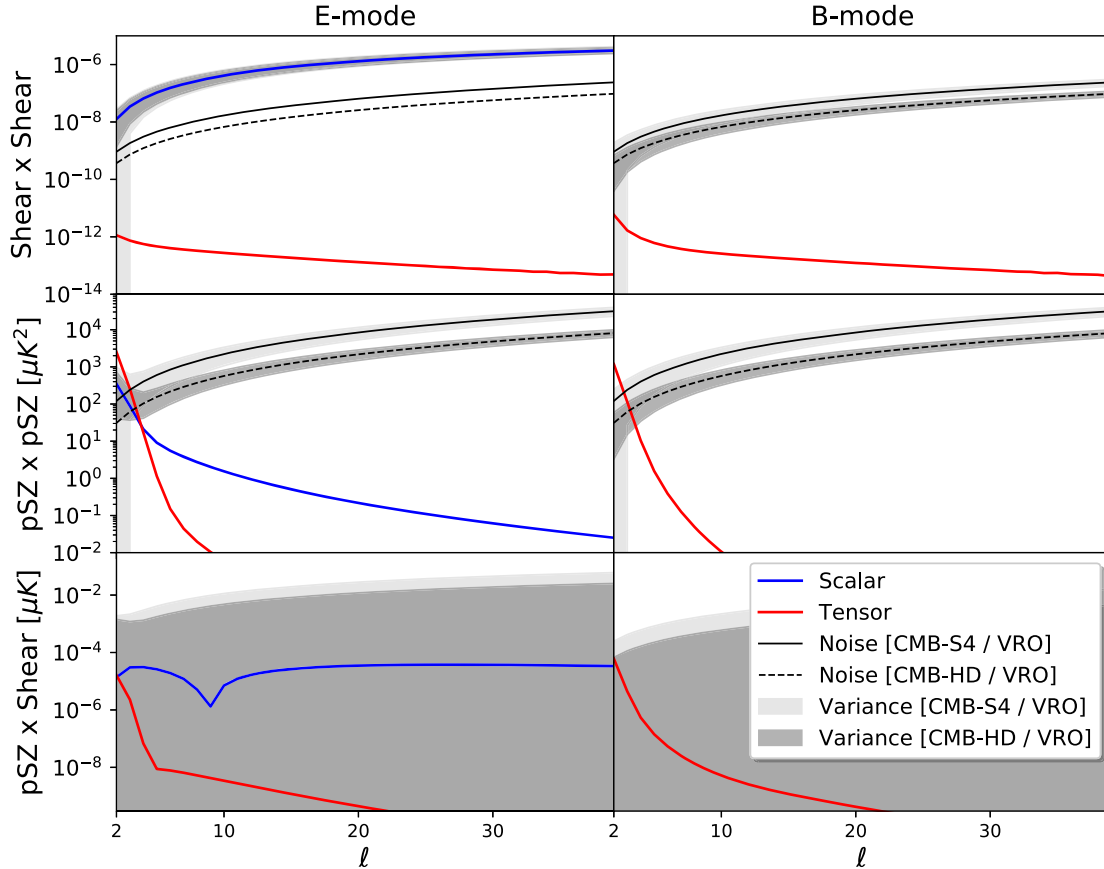


FIG. 2. Contributions of scalar and tensor modes to the shear and pSZ angular power spectrum. We show a single redshift bin centered at $z = 1$, and plot scalar (tensor) contributions to the spectra in blue (red, assuming $r = 1$). The first, second, and third plots show the shear-auto, pSZ-auto and shear-pSZ spectra for E modes (left) and B modes (right), with all spectra multiplied by $\ell(\ell + 1)/(2\pi)$. We additionally convert the CMB based measurements into micro-Kelvin units by multiplying by T_{CMB} . The black curves show noise contributions, and the gray regions give 1σ errors around the total tensor-free signal, relevant for both CMB-S4/VRO and CMB-HD/VRO experiments. Clearly, the pSZ-shear cross-spectra has much reduced signal to noise compared to the pSZ-pSZ spectra, though some detection of gravitational waves may be possible in the B mode, particularly at larger z .

The cross-spectra paint a somewhat different picture. In this case, there is no experimental noise curve (since $\langle E \rangle = \langle B \rangle = 0$ in the CMB), but significant variance, even for futuristic experimental setups based on CMB-HD. That said, both scalar and tensor contributions are clearly non-zero, with the latter peeking above the cosmic variance in the large-scale B mode. As discussed below, the various contributions are a strong function of redshift, but the trend of Fig. 2 is relatively general: both scalar and tensor cross-spectra exist but will be difficult to detect. This is quantified in the following sections.

In Fig. 3 we consider the cross-spectra in more detail, displaying results at both low and high redshift, and splitting the sample into the various contributions. At low redshifts, we see that the scalar contribution is dominated by the ISW effect, and contains power across a range of multipoles. This differs significantly from the pSZ auto-spectra, which is dominated by the SW effect and has power only at very low ℓ . In principle, this suggests that the low-redshift shear-pSZ (or galaxy-pSZ) correlation could be a useful probe of the ISW effect. At higher redshifts, this is no longer the case; we find that the SW effect dominates over ISW, with the Doppler contribution being significantly suppressed regardless of redshift. This is as expected: the ISW effect occurs due to the time variation of gravitational potentials induced by dark energy, whose action is strongly suppressed for $z \gtrsim 2$. The signature of tensors appears similar to scalars: the most prominent signatures are observed at low ℓ , and, partly due to the greater impact of tensors on high- z lensing, is most prominent at the largest redshifts. Finally, we consider the contribution of different lensing contributions: as shown in the figure, the scalar high- z sample is dominated by the lensing correlations, cf. [32], whilst for scalars at low- z and for tensors at all redshifts, intrinsic alignments

are an important contributor to the signal, although we caution that they are accompanied by a poorly understood bias parameter $b_T(\chi)$.

B. Detectability of scalar pSZ

To forecast the detection strength of pSZ we perform a Fisher forecast utilizing both the pSZ auto- and cross-spectra. For this purpose, we rescale the pSZ signal as $q^E \rightarrow (\alpha/\sqrt{2})q^E$, such that a Fisher forecast for α about $\alpha = 1$ gives the desired signal-to-noise ratio (setting $\alpha = 0$ in the covariance, i.e., working under null assumptions). The following spectra contain scalar pSZ signatures:

$$(\alpha^2/2)C_\ell^{q^E q^E}, \quad (\alpha/\sqrt{2})C_\ell^{q^E \gamma^E}, \quad (\alpha/\sqrt{2})C_\ell^{q^E g}; \quad (31)$$

these form the derivative vector in (30) (summing over bins and multipoles). By considering only subcomponents of the pSZ spectra (cf. Sec. III), we can additionally quantify the detection significance of physical signals such as the ISW effect.

Our main results are given in Table I and Fig. 4, both for the fiducial CMB-S4/VRO survey considered above, and a more futuristic survey based on CMB-HD/VRO. In each case, the total pSZ auto-spectrum can be robustly extracted (at 8.3σ and 37σ respectively), and is dominated by the SW effect; the other contributions are unmeasurable except for the ISW effect with futuristic noise levels. The signal-to-noise curves are a strong function of ℓ : only the $\ell \lesssim 5$ modes are recoverable by these techniques.

The situation is more bleak for the cross-spectra. Combining pSZ and photometric galaxy density does not yield an observable signal for either choice of noise curves, and, further, the pSZ-shear correlation is small ($\approx 1.6\sigma$) for CMB-S4/VRO noise levels. Further in the

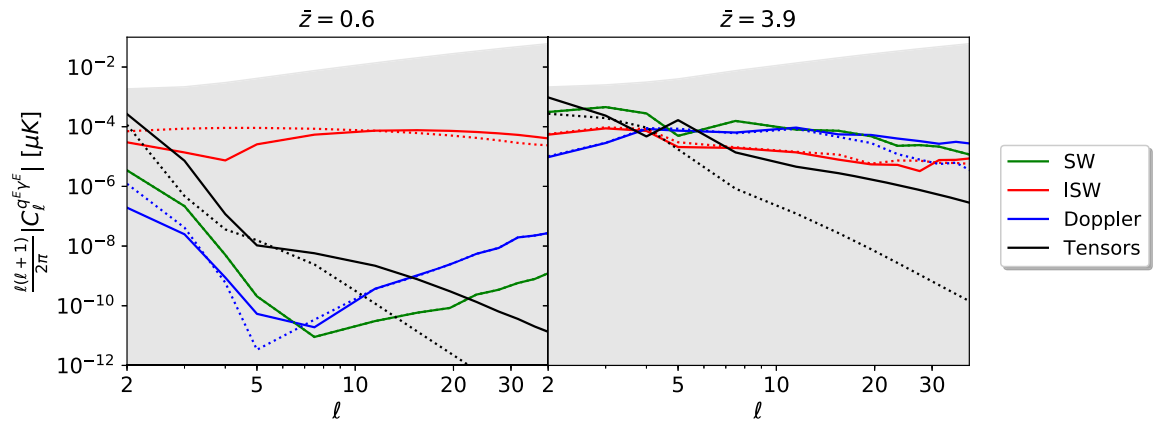


FIG. 3. Contributions to the E -mode pSZ-shear cross-spectrum in two redshift bins, with centers indicated by the titles. We show scalar contributions from the Sachs-Wolfe (green, SW), integrated Sachs-Wolfe (red, ISW) and Doppler (blue) effect and $r = 1$ tensors (black, as in Fig. 2). The dotted lines show the same contributions but only including the effects of gravitational lensing (omitting intrinsic alignments). The shaded region shows the 1σ error for VRO/CMB-S4 as in Fig. 2. We note that the ISW effect dominated the scalar signal at low- z , but there is significant contribution from the SW effect at high z . Furthermore, intrinsic alignments are seen to be a key contribution to the tensor signal in both bins, though the high- z scalar signals are sourced almost entirely by lensing shear modes.

TABLE I. Signal-to-noise ratio of the scalar pSZ effect from auto- and cross-spectra with shear and galaxies. We split the signal into various components, and compute the signal to noise using the Fisher formalism of (30), assuming zero fiducial pSZ signal. Results are shown for two choices of CMB noise (Δ_p , in $\mu\text{K-arcmin}$) and source density (\bar{n} , in arcmin^{-2}). We find that future surveys will be able to detect the pSZ auto-spectrum at high significance (sourced by the SW effect), but cross-spectra with galaxies are practically unobservable, and those with shear are weak, though dominated by the ISW effect.

	Δ_p	\bar{n}	SW	ISW	Doppler	Total
pSZ \times pSZ	1	40	12.59	0.58	0.05	8.40
pSZ \times shear	1	40	0.91	1.61	0.06	1.58
pSZ \times galaxies	1	40	0.42	0.61	0.07	0.65
pSZ \times pSZ	0.5	100	56.42	2.49	0.24	37.74
pSZ \times shear	0.5	100	3.32	5.18	0.21	5.16
pSZ \times galaxies	0.5	100	1.07	1.33	0.18	1.44

future however, we forecast a detection significance of 5.2σ for this cross-correlation using CMB-HD/VRO, which is dominated by the ISW effect. Noticeably, the decay of the signal to noise in cross-spectra is weaker than for auto-spectra; this indicates how more modes could be measured if the noise was particularly suppressed. Although the overall signal to noise is weak, it indicates how one, at least in principle, can extract the ISW effect from the usually SW-dominated pSZ signal by utilizing cross-correlations.

It is important to ask whether these results depend on the redshift binning strategy adopted. To this end, we have performed an analogous Fisher forecast using 30 tomographic bins rather than six, each with a width of

$\approx 300 h^{-1} \text{Mpc}$. Though such narrow bins are unlikely to be used in future optical surveys (due to photometric redshift uncertainties), they show how our results depend on the pSZ binning, and, for the galaxy cross-correlations, give an indication of how a spectroscopic survey would perform. In this case, we find very similar detection significances for all quantities, with an enhancement only at the $\lesssim 20\%$ level when using fine bins. In particular, the total pSZ-shear correlation can be detected at 1.8σ (4.5σ), whilst the pSZ-galaxy correlation becomes 0.8σ (1.8σ) for CMB-S4/VRO (CMB-HD/VRO). We may similarly assess the dependence on the maximum survey redshift: we find only a small ($\lesssim 10\%$) loss of signal to noise from reducing the redshift range to $[0.1, 2]$ instead of $[0.1, 6]$. This is due to the paucity of high-redshift objects in the fiducial sample. Altogether, the two tests indicate that six redshift bins are likely sufficient in practice, and that bins containing very few galaxies do not contribute significantly. Furthermore, we find that galaxy density is unlikely to be of practical use for measuring cross-correlations with pSZ, even if one uses a spectroscopic sample. Though the galaxy density field has lower noise than the shear observable (for photometric samples; far fewer sources are typically observed in spectroscopic analyses), the signal to noise of the cross-spectrum is dominated by modes in the linear regime (Fig. 4), which are instead cosmic-variance dominated. The difference in signal-to-noise indicates that the redshift kernel intrinsic to the remote quadrupole has better overlap with that from cosmic shear than galaxy density, and the limited impact of binning indicates that the signal is smooth in redshift and dominated by modes perpendicular to the line of sight.

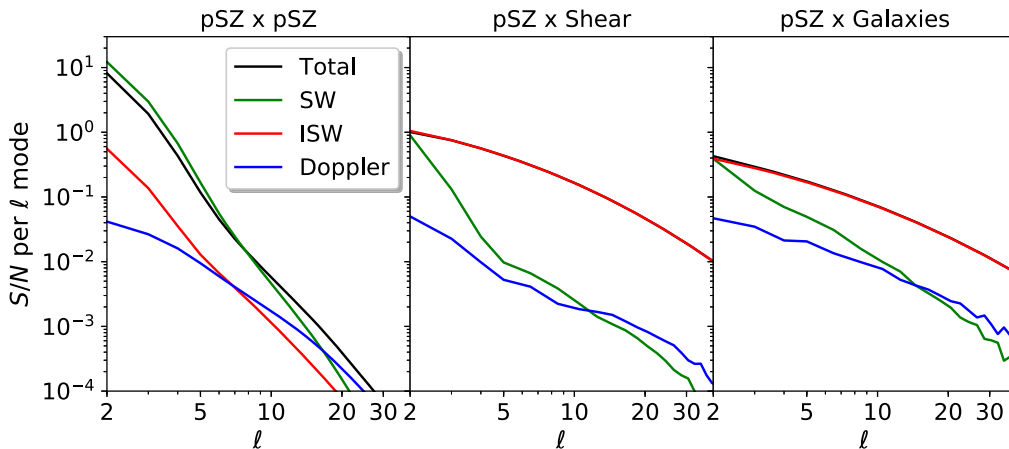


FIG. 4. Signal-to-noise (S/N) ratio for the pSZ auto- and cross-spectra. We give the significance of a detection in each ℓ bin [equivalent to the S/N per $\{\ell, m\}$ mode multiplied by $(2\ell + 1)$] the total S/N is the sum over all bins and given in Table I. We show detection significances for the total pSZ effect (black) and split into the SW, ISW and Doppler subcomponents (green, red, and blue), always assuming the CMB-S4/VRO noise parameters. The overall signal is strongest in the auto-spectrum; however, this is more susceptible to systematic effects than cross-spectra. The auto-spectra are dominated by the SW signal, whilst cross-spectra are a probe instead of the ISW. Whilst all curves are a strong function of ℓ , the falloff is slower for the cross-spectra, indicating the utility of measuring smaller scales.

TABLE II. 1σ error bar on the amplitude of parity-even (left) and parity-odd (right) tensors, r and $r\Delta_h$, from the pSZ and shear datasets, computed via the Fisher matrix formalism of (30). Results are shown for two noise parameters, as in Table I. We consider constraints from both lensing and intrinsic alignment (IA) contributions to the shear signal, which we note give significant cancellation. Odd-parity constraints involving shear are significantly tighter than those for even-parity spectra since the EB spectra are not cosmic-variance limited in linear theory. As in previous work, the constraining power of shear auto-spectra is very weak, but the cross-spectra offer a potential avenue for detecting tensors, albeit in the distant future.

$\sigma(r)$	Δ_P	\bar{n}	Lensing	IA	Total
(a) Even parity					
Shear \times Shear	1	40	190	114	51
pSZ \times pSZ	1	40	0.023
pSZ \times Shear	1	40	1.5	2.0	0.94
Shear \times Shear	0.5	100	66	39	17
pSZ \times pSZ	0.5	100	0.0050
pSZ \times Shear	0.5	100	0.42	0.54	0.26
$\sigma(r\Delta_h)$	Δ_P	\bar{n}	Lensing	IA	Total
(b) Odd parity					
Shear \times Shear	1	40	60	21	13
pSZ \times pSZ	1	40	0.046
pSZ \times Shear	1	40	0.18	0.46	0.22
Shear \times Shear	0.5	100	22	7.5	4.7
pSZ \times pSZ	0.5	100	0.012
pSZ \times Shear	0.5	100	0.050	0.15	0.055

C. Detectability of parity-even tensors

We now turn to gravitational waves, considering the possible bounds upcoming and futuristic surveys can place on the tensor-to-scalar ratio r . Whilst one could also probe the tensor tilt, n_T , this requires first measuring nonzero r , thus we will neglect it here (though see [11] for discussion of constraints from the pSZ auto-spectra). Assuming tensors are parity conserving, gravitational wave signatures appear in the following spectra, all proportional to r :

$$C_\ell^{q^E q^E}, \quad C_\ell^{q^B q^B}, \quad C_\ell^{\gamma^E \gamma^E}, \quad C_\ell^{q^E \gamma^E}, \quad C_\ell^{q^B \gamma^B}. \quad (32)$$

Importantly, this involves B modes which, via parity conservation, do not contain contributions from scalars at leading order, and thus provide a cleaner dataset within which to search for tensors. Additionally, there is no signal in the galaxy-pSZ cross-spectra (in linear theory), since the galaxy distribution is a scalar quantity.

The forecasted constraints on r are shown in Table II and Fig. 5. As found previously, e.g., [32], shear auto-spectra are not able to place tight constraints on tensors: even with the more optimistic noise profile, we find $\sigma(r) = 20$, several orders of magnitude weaker than the current constraints from BICEP [48]. This is partly caused by the VRO galaxy sample, whose source density peaks at $z \sim 0.3$ (albeit with a broad tail); a sample extending to higher z would allow for considerably more stringent limits.

For the pSZ-auto spectra, we find much tighter constraints, exceeding the current BICEP limits. Whilst these are unlikely to be competitive in the near future, given the rapid advance in CMB detector technology, e.g., [11], they are nevertheless interesting, since the signal arises from a small scale (doubly squeezed) $\langle \delta_g^2(Q \pm iU)^2 \rangle$ trispectrum rather than the usual $\langle BB \rangle$ signal, and is less subject to lensing and atmospheric effects. For the cross-spectra, we find weaker constraints, with a similar ℓ dependence to the auto-spectra. For CMB-S4/VRO, we forecast a 1σ constraint of $\sigma(r) = 0.9$ (in accordance with [11]), which increases only to 0.2 with the more optimistic noise profiles of CMB-HD/VRO. This is unlikely to be of use in the near future. Furthermore, the constraint scales with one power of the CMB noise amplitude, Δ_P (since the cross-spectrum involves only one polarization field), and thus improves slower than the auto-spectra when the noise is reduced (noting that the galaxy noise primarily arises from cosmic variance at low redshift, though, as before the situation is better at high redshift). Finally, we note that, unlike for shear, the pSZ-shear correlation arises primarily due to lensing effects, rather than intrinsic alignments, and is insensitive to the redshift binning, with $\lesssim 10\%$ change to $\sigma(r)$ if the number of bins is increased to 30.

D. Detectability of parity-odd tensors

Finally, we consider how one may measure the odd part of the tensor spectrum using the pSZ and shear. In this case, we require the following spectra:

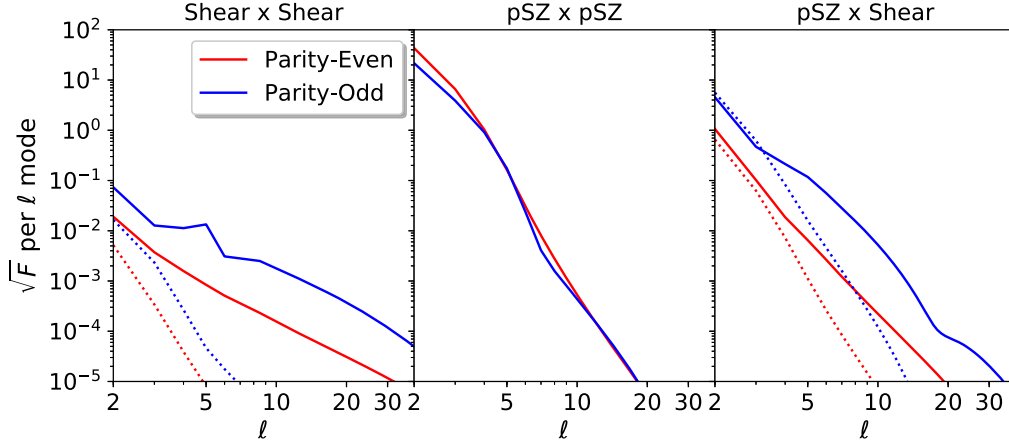


FIG. 5. Contributions to the tensor Fisher matrix from shear and pSZ auto- and cross-spectra, assuming CMB-S4/VRO noise parameters. We show results for the parity-even and parity-odd components (constraining r and $r\Delta_h$ respectively) in red and blue, plotting the contribution to $\sqrt{F} = \sigma^{-1}$ from each set of ℓ modes. The dashed curves give the results with only lensing shear modes; we find that lensing dominates the shear constraints, but intrinsic alignments are also important for the cross-spectra with pSZ. 1σ detection limits are given in Table II; briefly, we find that the cross-spectrum has some (albeit weak) sensitivity to tensors, particularly parity-odd tensors, and, suffers less from from systematic effects than auto-spectra.

$$C_\ell^{q^E q^B}, \quad C_\ell^{\gamma^E \gamma^B}, \quad C_\ell^{q^E \gamma^B}, \quad C_\ell^{q^B \gamma^E}, \quad (33)$$

each of which is proportional to the parity-odd amplitude $r\Delta_h$. Interestingly, none of the spectra involving γ^B suffer from cosmic variance limitations at leading order, since $\langle \gamma^B \gamma^B \rangle$ contains only noise. As such, we may expect the constraints on parity-odd components to be tighter than those on their even brethren.

Fisher forecasts for $r\Delta_h$ are given in the right panel of Table II and Fig. 5. As foretold, the shear-shear and pSZ-shear constraints on odd-parity tensors are significantly (around an order of magnitude) tighter than for even-parity tensors, but similar for the pSZ auto-spectra, since the relevant estimator involves both CMB E and B modes. That said, our conclusions are similar to before: the shear-auto spectra gives weak constraints, with $\sigma(r\Delta_h) = 13$ for CMB-S4/VRO, whilst the pSZ auto-spectra are somewhat tighter (0.05 for CMB-S4/VRO noise), though unlikely to be competitive in the near future. For the cross-spectra, we forecast $\sigma(r\Delta_h) = 0.2$ for CMB-S4/VRO, or 0.06 for CMB-HD/VRO. Whilst this is still weak, it may be interesting from the point of view of systematics, since the associated CMB primary measurements can often be marred by foregrounds.

VI. NOVEL COSMOLOGICAL TESTS

In the above, we have highlighted the unique properties of the pSZ-shear cross-correlation. In particular, at low redshifts the cross-spectrum isolates the ISW component of pSZ, whilst at high redshifts the SW component is picked

out (as in Fig. 1). Here, we explore the implications of these properties in the context of a toy model in order to develop some intuition for their utility.

Consider a primordial potential perturbation consisting of a single mode $\mathbf{k} = k_0 \hat{\mathbf{z}}$ with amplitude A . Ignoring radial binning, the multipole moments of an observable $X \in \{\delta_g, \gamma^E, q^E\}$ at fixed comoving distance χ are given by

$$a_{\ell m}^X(\chi) = \sqrt{\frac{2\ell+1}{4\pi}} A \Delta_\ell^X(k_0, \chi) \delta_{m0}^K, \quad (34)$$

where $\Delta_\ell^X(k_0, \chi)$ are the transfer functions defined in Appendix A. In the limit of noiseless measurements of each spectra, the ratio of multipole moments becomes a ratio of transfer functions:

$$\frac{a_{\ell 0}^X(\chi)}{a_{\ell 0}^Y(\chi)} = \frac{\Delta_\ell^X(k_0, \chi)}{\Delta_\ell^Y(k_0, \chi)}. \quad (35)$$

A. SW contributions

At high redshift, where ISW can be neglected, the ratio of the galaxy density to the remote quadrupole signal is

$$\frac{a_{\ell 0}^{\delta_g}(\chi)}{a_{\ell 0}^{q^E}(\chi)} \propto \frac{(k_0 \chi)^2}{j_2(k_0 [\chi_{\text{dec}} - \chi])} \times \frac{D_\Psi(\eta_0 - \chi)}{\left(2D_\Psi(\eta_{\text{dec}}) - \frac{3}{2}\right)}. \quad (36)$$

This is the product of a geometrical factor [which in the limit $k_0 \ll 1$ reduces to $\chi^2 / (\chi_{\text{dec}} - \chi)^2$] and a ratio of the potential growth functions at very different times, as

previously noted. The ratio of the E -mode shear to the remote quadrupole takes a similar form:

$$\frac{a_{\ell 0}^{\gamma^E, \text{IA}}(\chi)}{a_{\ell 0}^{q^E}(\chi)} \propto \frac{(k_0 H_0^{-1})^2}{j_2(k_0[\chi_{\text{dec}} - \chi])} \times \frac{D_{\Psi}(\eta_0 - \chi)}{\left(2D_{\Psi}(\eta_{\text{dec}}) - \frac{3}{2}\right)} \quad (37)$$

for intrinsic alignment, and

$$\frac{a_{\ell 0}^{\gamma^E, \text{lens}}(\chi)}{a_{\ell 0}^{q^E}(\chi)} \propto \int_0^\infty \frac{d\chi'}{\chi'} q_a(\chi') \frac{j_\ell(k\chi')}{j_\ell(k\chi)} \frac{(k\chi)^2}{j_2(k[\chi_{\text{dec}} - \chi])} \times \frac{D_{\Psi}(\eta_0 - \chi')}{\left(2D_{\Psi}(\eta_{\text{dec}}) - \frac{3}{2}\right)} \quad (38)$$

for the lensing contribution. Both of these contributions are also a geometrical factor (which is different from that appearing in the galaxy density expression) times a ratio of potential growth functions, with the lensing contributions weighted by comoving distance. Within this toy model, one could in principle measure the ratios above without cosmic variance, mapping out the geometry of the light cone and the potential growth function with arbitrary precision.

B. ISW contributions

At low redshifts the SW and Doppler terms can be neglected, and the ratio of galaxy density and the remote quadrupole multipoles becomes

$$\frac{a_{\ell 0}^{\delta_g}(\chi)}{a_{\ell 0}^{q^E}(\chi)} \propto \frac{(k_0\chi)^2 D_{\Psi}(\eta_0 - \chi)}{\int_{\chi}^{\chi_{\text{dec}}} d\bar{\chi} j_2(k_0[\bar{\chi} - \chi]) \partial_{\eta} D_{\Psi}(\eta_0 - \bar{\chi})} \sim \frac{(k_0\chi)^2}{j_2(k_0[\chi_{\text{dec}} - \chi])} \times \frac{D_{\Psi}(\eta_0 - \chi)}{D_{\Psi}(\eta_0 - \chi) - D_{\Psi}(\chi_{\text{dec}})} \quad (39)$$

which is a geometrical factor multiplying the fractional change in the potential growth function. The analogous ratio for shear and the remote quadrupole is

$$\frac{a_{\ell 0}^{\gamma^E, \text{IA}}(\chi)}{a_{\ell 0}^{q^E}(\chi)} \propto \frac{(k_0 H_0^{-1})^2 D_{\Psi}(\eta_0 - \chi)}{\int_{\chi}^{\chi_{\text{dec}}} d\bar{\chi} j_2(k_0[\bar{\chi} - \chi]) \partial_{\eta} D_{\Psi}(\eta_0 - \bar{\chi})} \sim \frac{(k_0 H_0^{-1})^2}{j_2(k_0[\chi_{\text{dec}} - \chi])} \times \frac{D_{\Psi}(\eta_0 - \chi)}{D_{\Psi}(\eta_0 - \chi) - D_{\Psi}(\chi_{\text{dec}})} \quad (40)$$

for intrinsic alignment and

$$\frac{a_{\ell 0}^{\gamma^E, \text{lens}}(\chi)}{a_{\ell 0}^{q^E}(\chi)} \propto \int_0^\infty \frac{d\chi'}{\chi'} q_a(\chi') \frac{j_\ell(k\chi')}{j_\ell(k\chi)} \times \frac{(k_0\chi')^2 D_{\Psi}(\eta_0 - \chi')}{\int_{\chi}^{\chi_{\text{dec}}} d\bar{\chi} j_2(k_0[\bar{\chi} - \chi]) \partial_{\eta} D_{\Psi}(\eta_0 - \bar{\chi})} \quad (41)$$

for lensing. Each of these ratios is dependent on the change in the potential growth function, which is sensitive to the properties of dark energy. Within the context of this toy model, it is therefore possible to put strong constraints on the properties of dark energy, which, due to the off-light-cone properties, are free from cosmic variance.

Extending beyond the toy model described above, information about the geometry of the light cone and the potential growth functions has a more complex encoding in the observables. Nevertheless, the above model illustrates the types of novel cosmological tests that may eventually be possible by combining pSZ and shear or density measurements.

VII. DISCUSSION

This work has considered a novel probe of cosmic history: the correlation of the polarized SZ effect with galaxy shear. Unlike most observables, this is not restricted to the light cone, and can capture interesting physics in both the scalar and tensor sectors, particularly with regards to the ISW effect and parity-odd gravitational waves. Despite significant theoretical and phenomenological appeal, this cross-correlation appears highly challenging to detect. With the forthcoming generation of surveys, a tenuous detection of the scalar signal may just be within reach, but it is unlikely that the signal can be fully exploited in either this decade or the next. That said, the effect's detectability is limited predominantly by CMB detector noise and the availability of high-redshift galaxies, both of which are likely to improve in the future (for example with MegaMapper [38], though the high-redshift tail is limited by reionization). We note an important caveat: this work has only considered linear contributions to the pSZ and shear statistics. In the nonlinear Universe, higher-order scalar corrections can lead to non-negligible contributions to both E - and B -mode observables, which may give a fundamental limitation to how well the various signals can be detected. Furthermore, we have ignored the notorious ‘‘optical depth degeneracy,’’ relating to the poorly understood connection between the electron and matter distributions, e.g., [8]. Whilst this is an important multiplicative uncertainty, the detections considered herein are sufficiently futuristic that one may cautiously hope such problems to be solved by the relevant time, for example using kSZ measurements or cross-correlations with fast radio bursts [49].

Putting the above issues aside, we close by considering the implications of a detection of the pSZ-shear cross-correlation, assuming that one can be made. Perhaps the most appealing feature of cross-correlations is that they suffer from significantly fewer systematic effects than auto-spectra. As mentioned above, the pSZ-shear spectra is a $\langle \gamma \delta(Q \pm iU) \rangle$ bispectrum, and involves only one power of the CMB: as such, a number of physical effects, including detector noise and calibration errors, will be averaged out. In particular, galactic foregrounds and weak lensing provide serious barriers to extracting tensor modes from the primary CMB: the former contributes only if a residual galaxy selection function couples to the galactic microwave emission, whilst the latter generally cancels in the pSZ signal, due to the structure of the relevant kernel [11]. Although the constraining power on tensor modes from pSZ is weak, the availability of such a constraint may be an important cross-check in the event of a future detection of tensors from the primary CMB.

Second, we have shown that the pSZ-shear cross-correlation is dominated by the ISW effect (unlike pSZ auto-spectra), particularly at low redshifts. Although a robust detection remains far off, its measurement would provide direct evidence for dark energy, inducing the time variation of the Bardeen potentials. Usual ISW constraints arising from the CMB (mostly commonly via cross-correlations, e.g., [50–52]) are fundamentally limited by cosmic variance, thus, the pSZ-based measurements, which can recover three-dimensional modes instead of the usual two-dimensional ones, may provide a useful avenue for an eventual high-significance measurement of the properties of dark energy. Finally, the measurement of the SW effect in the pSZ-shear cross-spectra (which is most prominent at high redshifts), would give a unique insight into the Universe’s (in)homogeneous evolution. For a lens at χ , the pSZ-shear cross-spectrum measures the following combination of growth rates: $D(\chi, \mathbf{x})D(\chi_{\text{dec}}, \mathbf{x})$ (ignoring a geometric prefactor), which can be compared to that of lensing alone: $D^2(\chi, \mathbf{x})$, at some position \mathbf{x} . As mentioned above, a futuristic measurement could, in principle, be used to map the local (off-light-cone) values of $D(\chi, \mathbf{x})/D(\chi_{\text{dec}}, \mathbf{x})$ without cosmic variance, allowing novel tests of the Universe’s isotropy and homogeneity, for example probing whether the Universe evolves differently in high- and low-density regions.

Although difficult in practice, a measurement of the pSZ-shear cross-correlation could probe a range of new physics, and shed light on new and unexplored features of the cosmological model.

ACKNOWLEDGMENTS

We thank Jo Dunkley, Vid Irsic, Blake Sherwin, Kendrick Smith and the participants of the Flatiron SZ workshop for insightful discussions relating to pSZ, as well as Stephon Alexander, Morgane König, and David Spergel for discussions on galaxy shape statistics. We are also grateful to the anonymous referee for an insightful report. O. H. E. P. acknowledges support of the Simons Society of Fellows and thanks the Perimeter Institute for supporting a visit within which this work was conceived as well as the Simons Foundation and Institute for Advanced Study for support. M. C. J. is supported by the National Science and Engineering Research Council through a Discovery grant. This research was supported in part by Perimeter Institute for Theoretical Physics. Research at Perimeter Institute is supported by the Government of Canada through the Department of Innovation, Science and Economic Development Canada and by the Province of Ontario through the Ministry of Research, Innovation and Science.

The authors are pleased to acknowledge that the work reported in this paper was substantially performed using the Research Computing resources at Princeton University which is a consortium of groups led by the Princeton Institute for Computational Science and Engineering (PICSciE) and the Office of Information Technology’s Research Computing.

APPENDIX A: TRANSFER FUNCTIONS

In this appendix, we collect the transfer functions necessary to compute the signal spectra in Eqs. (21) and (22). Starting with the galaxy density defined in Eq. (15), which is sourced only by scalars at linear order, we have

$$i^{-\ell} \Delta_{\ell,a}^{\delta_g, S}(k) = - \int_0^\infty d\chi n_a(\chi) \frac{2a(\chi)k^2}{3H_0^2 \Omega_m} b_g(\chi) \times D_\Psi(\eta_0 - \chi) j_\ell(k\chi). \quad (\text{A1})$$

Since our primary goal is to compute the SZ-lensing cross-correlations, we do not pursue a detailed accounting of redshift space distortions, magnification, or relativistic corrections to the observed number counts. A discussion of these effects and their correlations with SZ effects can be found in [53].

Moving to shear, the scalar contribution to the E mode defined in Eq. (17) has the transfer function

$$\Delta_{\ell,a}^{qE,S}(k) = i^\ell \sqrt{\frac{(\ell+2)!}{(\ell-2)!}} \left[- \int_0^\infty d\chi n_a(\chi) \frac{b_S(\chi)}{2\chi^2} D_\Psi(\eta_0 - \chi) j_\ell(k\chi) + \int_0^\infty \frac{d\chi'}{\chi'} q_a(\chi') D_\Psi(\eta_0 - \chi') j_\ell(k\chi') \right], \quad (\text{A2})$$

where the lensing efficiency is $q_a(\chi') \equiv \int_{\chi'}^\infty d\chi n_a(\chi)$. The tensor contributions to the E - and B -mode shear defined in Eq. (18) have the transfer functions for $X \in \{E, B\}$ ⁹:

$$\begin{aligned} -i^{-\ell} \Delta_{\ell,a}^{rX,T}(k) &= -\frac{1}{8} \mathcal{O}_X[\hat{Q}_{\text{IA,T}}(x)] \frac{j_\ell(x)}{x^2} \Big|_{x=0} D_T(k, \eta_0) \\ &\quad - \frac{1}{8} \int_0^\infty d\chi n_a(\chi) \mathcal{O}_X[\hat{Q}_{\text{IA,T}}(x)] \frac{j_\ell(x)}{x^2} (1 - b_T(\chi) a^{-2}(\chi) (\partial_\eta^2 + aH\partial_\eta)) D_T(k, \eta_0 - \chi) \\ &\quad + \frac{1}{4} \int_0^\infty \frac{d\chi'}{\chi'} (m_a(\chi') \mathcal{O}_X[\hat{Q}_{\text{lens,T,1}}(x')] + \bar{m}_a(\chi') \mathcal{O}_X[\hat{Q}_{\text{lens,T,2}}(x')]) \frac{j_\ell(x')}{x'^2} D_T(k, \eta_0 - \chi'), \end{aligned} \quad (\text{A3})$$

where we define

$$m_a(\chi') = \int_{\chi'}^\infty d\chi n_a(\chi), \quad \bar{m}_a(\chi') = \int_{\chi'}^\infty d\chi \frac{\chi'}{\chi} n_a(\chi), \quad (\text{A4})$$

and we have $\mathcal{O}_E = \text{Re}$, $\mathcal{O}_B = \text{Im}$, $x \equiv k\chi$, $x' \equiv k\chi'$, and D_T is the tensor growth factor, defined after (9). This uses the operators

$$\begin{aligned} \hat{Q}_{\text{lens,T,1}}(x) &= -\frac{x}{2} [x(x^2 + 14) + 2(7x^2 + 20)\partial_x + 2x(x^2 + 25)\partial_x^2 + 14x^2\partial_x^3 + x^3\partial_x^4 - 2i(4 + x^2 + 6x\partial_x + x^2\partial_x^2)] \\ \hat{Q}_{\text{lens,T,2}}(x) &= \frac{1}{2} [24(x^2 + 1) + x^4 + 16x(x^2 + 6)\partial_x + 2x^2(x^2 + 36)\partial_x^2 + 16x^3\partial_x^3 + x^4\partial_x^4], \\ \hat{Q}_{\text{IA,T}}(x) &= [12 - x^2 + 8x\partial_x + x^2\partial_x^2] + 2ix[4 + x\partial_x], \end{aligned} \quad (\text{A5})$$

which act on the spherical Bessel functions.¹⁰

For the remote quadrupole field we follow [10,11]. The E -mode remote quadrupole sourced by scalars is given by¹¹

$$\Delta_{\ell,a}^{qE,S}(k) = - \int_0^\infty d\chi n_a(\chi) 5i^\ell \sqrt{\frac{3}{8}} \sqrt{\frac{(\ell+2)!}{(\ell-2)!}} \frac{j_\ell(k\chi)}{(k\chi)^2} [\mathcal{G}_{\text{SW}} + \mathcal{G}_{\text{ISW}} + \mathcal{G}_{\text{Doppler}}](k, \chi), \quad (\text{A6})$$

where

$$\begin{aligned} \mathcal{G}_{\text{SW}}(k, \chi) &= - \left(2D_\Psi(\eta_{\text{dec}}) - \frac{3}{2} \right) j_2(k[\chi_{\text{dec}} - \chi]) \\ \mathcal{G}_{\text{ISW}}(k, \chi) &= -2 \int_\chi^{\chi_{\text{dec}}} d\bar{\chi} \partial_\eta D_\Psi(\bar{\eta}) j_2(k[\bar{\chi} - \chi]) \\ \mathcal{G}_{\text{Doppler}}(k, \chi) &= \frac{1}{5} k D_v(\eta_{\text{dec}}) (3j_3(k[\chi_{\text{dec}} - \chi]) - 2j_1(k[\chi_{\text{dec}} - \chi])). \end{aligned} \quad (\text{A7})$$

The pSZ effect is also sourced by gravitational waves, with the same structure as (19) but encoding the tensorial contributions to Θ , arising from post-recombination effects, as in the usual CMB. Following a lengthy calculation outlined in [10,11], we find the following transfer functions:

⁹This matches [32,54], albeit with slightly modified conventions described in Sec. II B.

¹⁰These, respectively, correspond to $2\hat{Q}_2^*(x)$, $2\hat{Q}_3^*(x)$, and $\hat{Q}_1^*(x)$ in the notation of [32].

¹¹In full, the pSZ signal contains two effects: (a) contributions arising from the remote quadrupole observed at the galaxy location, and (b) contributions sourced by photon distortions between scattering and the observer. The second set are higher-order effects (since they are unobservable unless the first is also present), and will be neglected herein.

$$\begin{aligned}
 i^{-\ell} \Delta_{\ell,a}^{q^E,T}(k) &= \int_0^\infty d\chi n_a(\chi) \frac{5\sqrt{6}}{4} \text{Re}[\hat{Q}_{\text{IA},T}(x)] \frac{j_\ell(x)}{x^2} \int_\chi^{\chi_{\text{dec}}} d\bar{\chi} \partial_\eta D_T(\bar{\eta}) \frac{j_2(k[\bar{\eta} - \eta])}{(k[\bar{\eta} - \eta])^2} \\
 i^{-\ell} \Delta_{\ell,a}^{q^B,T}(k) &= - \int_0^\infty d\chi n_a(\chi) \frac{5\sqrt{6}}{4} \text{Im}[\hat{Q}_{\text{IA},T}(x)] \frac{j_\ell(x)}{x^2} \int_\chi^{\chi_{\text{dec}}} d\bar{\chi} \partial_\eta D_T(\bar{\eta}) \frac{j_2(k[\bar{\eta} - \eta])}{(k[\bar{\eta} - \eta])^2}, \tag{A8}
 \end{aligned}$$

in terms of the $\hat{Q}_{\text{IA},T}$ operator of (A5).

APPENDIX B: CORRELATIONS WITH THE KINETIC SUNYAEV-ZEL'DOVICH EFFECT

In the above, we have considered the correlations between galaxy shear and the polarized SZ effect. It is interesting to ask also if one expects correlations with the *kinetic* SZ effect (kSZ), given that this is observed at much higher signal to noise. Much as the pSZ probes a remote quadrupole, the kSZ effect probes a remote dipole, given by

$$v_{\text{eff}}(\chi \hat{n}) = \frac{3}{4\pi} \int d\hat{n} \Theta(\chi \hat{n}, \hat{n}') (\hat{n}' \cdot \hat{n}), \tag{B1}$$

where Θ is the CMB temperature fluctuation observed at the location of a distant galaxy. The dipole can be estimated by combining the observed CMB temperature with a tracer of the electron density, with the schematic form

$$\hat{v}_{\ell m,a} = \sum_{\ell_1 m_1 \ell_2 m_2} W_{\ell m \ell_1 m_1 \ell_2 m_2}^T a_{\ell_1 m_1}^T \Delta \tau_{\ell_2 m_2, a}, \tag{B2}$$

where W^T is some weight matrix, $a_{\ell m}^T$ are the CMB harmonics and $\Delta \tau_a$ is the Thomson cross section in bin a . This probes the combination $\delta_g T$, such that its auto power spectrum is $\langle \delta_g^2 T^2 \rangle$ and its cross-spectrum with shear is a $\langle \gamma \delta_g T \rangle$ bispectrum.

1. Formalism

Following Sec. III, the remote dipole power spectrum is given by (from [10], adapting to our conventions)

$$\begin{aligned}
 C_{\ell}^{vv}(\chi, \chi')|_S &= 4\pi \int_0^\infty d \log k \Delta_{\ell}^{v,S}(k, \chi) \Delta_{\ell}^{v,S*}(k, \chi') \\
 &\times \mathcal{P}_\Psi(k) \quad (\ell \geq 1). \tag{B3}
 \end{aligned}$$

Unlike for the remote quadrupole, there are no tensor contributions at leading order, since v is a spin-1 field. This defines the kernels,

$$\begin{aligned}
 i^{-\ell} \Delta_{\ell}^{v,S}(k, \chi) &= \frac{1}{2\ell + 1} [\mathcal{K}_{\text{SW}} + \mathcal{K}_{\text{ISW}} + \mathcal{K}_{\text{Doppler}}] \\
 &\times (k, \chi) [\ell j_{\ell-1}(k\chi) - (\ell + 1)j_{\ell+1}(k\chi)], \tag{B4}
 \end{aligned}$$

with

$$\begin{aligned}
 \mathcal{K}_{\text{SW}}(k, \chi) &= 3 \left(2D_\Psi(\eta_{\text{dec}}) - \frac{3}{2} \right) j_1(k[\chi_{\text{dec}} - \chi]) \\
 \mathcal{K}_{\text{ISW}}(k, \chi) &= 6 \int_\chi^{\chi_{\text{dec}}} d\bar{\chi} \partial_\eta D_\Psi(\bar{\eta}) j_1(k[\bar{\chi} - \chi]) \\
 \mathcal{K}_{\text{Doppler}}(k, \chi) &= k D_v(\eta_{\text{dec}}) (j_0(k[\chi_{\text{dec}} - \chi]) - 2j_2(k[\chi_{\text{dec}} - \chi])) - k D_v(\eta). \tag{B5}
 \end{aligned}$$

These can be integrated in redshift as before.

Finally, we require the noise profile of the remote dipole:

$$\frac{1}{C_{\ell}^{vv}(\chi, \chi')|_{\text{noise}}} = \frac{\delta_D(\chi - \chi')}{2\ell + 1} \sum_{\ell_1 \ell_2} \frac{\Gamma_{\ell \ell_1 \ell_2}^{\text{kSZ}}(\chi) \Gamma_{\ell \ell_1 \ell_2}^{\text{kSZ}}(\chi')}{C_{\ell_1}^{TT} C_{\ell_2}^{\delta_g \delta_g}(\chi, \chi')} \tag{B6}$$

or, after binning in redshift,

$$\frac{1}{C_{\ell,ab}^{vv}|_{\text{noise}}} = \frac{\delta_K^{ab}}{2\ell + 1} \sum_{\ell_1 \ell_2} \frac{\Gamma_{\ell \ell_1 \ell_2, a}^{\text{kSZ}} \Gamma_{\ell \ell_1 \ell_2, b}^{\text{kSZ}}}{C_{\ell_1}^{TT} C_{\ell_2, ab}^{\delta_g \delta_g}} \tag{B7}$$

with the definition

$$\begin{aligned}
 \Gamma_{\ell \ell_1 \ell_2}^{\text{kSZ}}(\chi) &= \sqrt{\frac{(2\ell_1 + 1)(2\ell_2 + 1)(2\ell + 1)}{4\pi}} \\
 &\times \begin{pmatrix} \ell_1 & \ell_2 & \ell \\ 0 & 0 & 0 \end{pmatrix} C_{\ell_2}^{\Delta \tau \delta_g}(\chi). \tag{B8}
 \end{aligned}$$

2. Forecasts

To estimate the utility of the kSZ-shear cross-correlation we utilize Fisher forecasts, as in Sec. V. Here, only shear correlations are of relevance (from the SW, ISW and

Doppler effects), and we show the corresponding detection significances in Table III. The kSZ auto-spectrum can be detected at high signal to noise in future surveys (which is of no surprise, given that it has been detected in current surveys), with strong detections of both the kSZ-shear and kSZ-galaxy cross-correlations also expected. In contrast to the pSZ signal, the kSZ correlators are dominated by the Doppler term (arising primarily from the source's peculiar velocity); this arises from physics *on* the light cone, and thus does not add new modes of interest. In the auto-spectra, there is a significant contribution from the SW effect, however, this is reduced from the cross-spectra, with a lower signal to noise found even than for pSZ. We note that these results are sensitive to the redshift binning: increasing to 30 tomographic bins (without photometric errors) roughly doubles the signal to noise of the auto-spectra, and amplifies the kSZ-galaxy cross-correlation to a value more comparable with the auto-spectrum. All in all, we conclude that the kSZ cross-spectra are not of particular use if one is interested in off-light-cone

TABLE III. As Table I but for the kSZ signal. We find that future surveys will be able to detect both kSZ auto- and cross-spectra at high significance, but that these are strongly dominated by the Doppler velocity term, with the other (off-light-cone) contributions being suppressed even relative to the pSZ case. Both auto- and cross-spectra are significantly enhanced when the number of tomographic bins is increased.

	Δ_p	\bar{n}	SW	ISW	Doppler	Total
kSZ \times kSZ	1	40	4.2	0.28	440	440
kSZ \times shear	1	40	0.39	0.48	77	77
kSZ \times galaxies	1	40	0.24	0.41	38	38
kSZ \times kSZ	0.5	100	32	2.0	3200	3200
kSZ \times shear	0.5	100	1.8	2.2	350	350
kSZ \times galaxies	0.5	100	0.78	1.20	110	110

physics. However, the large Doppler term may be of use in other contexts, for example in breaking the optical depth degeneracy via a joint shear and kSZ 3×2 -point analysis.

-
- [1] R. Maartens, Is the Universe homogeneous?, *Phil. Trans. R. Soc. A* **369**, 5115 (2011).
- [2] P. Zhang and M. C. Johnson, Testing eternal inflation with the kinetic Sunyaev Zel'dovich effect, *J. Cosmol. Astropart. Phys.* **06** (2015) 046.
- [3] A. Terrana, M.-J. Harris, and M. C. Johnson, Analyzing the cosmic variance limit of remote dipole measurements of the cosmic microwave background using the large-scale kinetic Sunyaev Zel'dovich effect, *J. Cosmol. Astropart. Phys.* **02** (2017) 040.
- [4] R. A. Sunyaev and Y. B. Zeldovich, The velocity of clusters of galaxies relative to the microwave background. The possibility of its measurement, *Mon. Not. R. Astron. Soc.* **190**, 413 (1980).
- [5] E. Audit and J. F. L. Simmons, The kinematic Sunyaev Zel'dovich effect and transverse cluster velocities, *Mon. Not. R. Astron. Soc.* **305**, L27 (1999).
- [6] A. Challinor, M. Ford, and A. Lasenby, Thermal and kinematic corrections to the microwave background polarization induced by galaxy clusters along the line of sight, *Mon. Not. R. Astron. Soc.* **312**, 159 (2000).
- [7] J. Shao, P. Zhang, W. Lin, Y. Jing, and J. Pan, The kinetic SZ tomography with spectroscopic redshift surveys, *Mon. Not. R. Astron. Soc.* **413**, 628 (2011).
- [8] K. M. Smith, M. S. Madhavacheril, M. Münchmeyer, S. Ferraro, U. Giri, and M. C. Johnson, KSZ tomography and the bispectrum, [arXiv:1810.13423](https://arxiv.org/abs/1810.13423).
- [9] S. Y. Sazonov and R. A. Sunyaev, Microwave polarization in the direction of galaxy clusters induced by the CMB quadrupole anisotropy, *Mon. Not. R. Astron. Soc.* **310**, 765 (1999).
- [10] A.-S. Deutsch, E. Dimastrogiovanni, M. C. Johnson, M. Münchmeyer, and A. Terrana, Reconstruction of the remote dipole and quadrupole fields from the kinetic Sunyaev Zel'dovich and polarized Sunyaev Zel'dovich effects, *Phys. Rev. D* **98**, 123501 (2018).
- [11] A.-S. Deutsch, E. Dimastrogiovanni, M. Fasiello, M. C. Johnson, and M. Münchmeyer, Primordial gravitational wave phenomenology with polarized Sunyaev Zel'dovich tomography, *Phys. Rev. D* **100**, 083538 (2019).
- [12] A.-S. Deutsch, M. C. Johnson, M. Münchmeyer, and A. Terrana, Polarized Sunyaev Zel'dovich tomography, *J. Cosmol. Astropart. Phys.* **04** (2018) 034.
- [13] N. Itoh, S. Nozawa, and Y. Kohyama, Relativistic corrections to the Sunyaev-Zel'dovich effect for clusters of galaxies. 3. Polarization effect, *Astrophys. J.* **533**, 588 (2000).
- [14] M. S. Emritte, S. Colafrancesco, and P. Marchegiani, Polarization of the Sunyaev-Zel'dovich effect: Relativistic imprint of thermal and nonthermal plasma, *J. Cosmol. Astropart. Phys.* **07** (2016) 031.
- [15] E. Alizadeh and C. M. Hirata, How to detect gravitational waves through the cross-correlation of the galaxy distribution with the CMB polarization, *Phys. Rev. D* **85**, 123540 (2012).
- [16] M. Kamionkowski and A. Loeb, Getting around cosmic variance, *Phys. Rev. D* **56**, 4511 (1997).
- [17] A. Hall and A. Challinor, Detecting the polarization induced by scattering of the microwave background quadrupole in galaxy clusters, *Phys. Rev. D* **90**, 063518 (2014).
- [18] N. Seto and M. Sasaki, Polarization signal of distant clusters and reconstruction of primordial potential fluctuations, *Phys. Rev. D* **62**, 123004 (2000).

- [19] L. R. Abramo and H. S. Xavier, Real space tomography of the primordial Universe with cluster polarization, *Phys. Rev. D* **75**, 101302 (2007).
- [20] E. F. Bunn, Probing the Universe on gigaparsec scales with remote cosmic microwave background quadrupole measurements, *Phys. Rev. D* **73**, 123517 (2006).
- [21] G.-C. Liu, K. Ichiki, H. Tashiro, and N. Sugiyama, Reconstruction of CMB temperature anisotropies with primordial CMB induced polarization in galaxy clusters, *Mon. Not. R. Astron. Soc.* **460**, L104 (2016).
- [22] J. Portsmouth, Analysis of the Kamionkowski-Loeb method of reducing cosmic variance with CMB polarization, *Phys. Rev. D* **70**, 063504 (2004).
- [23] D. Baumann and A. Cooray, CMB-induced cluster polarization as a cosmological probe, *New Astron. Rev.* **47**, 839 (2003).
- [24] N. Seto and E. Pierpaoli, Probing the Largest Scale Structure in the Universe with Polarization Map of Galaxy Clusters, *Phys. Rev. Lett.* **95**, 101302 (2005).
- [25] Z. Pan and M. C. Johnson, Forecasted constraints on modified gravity from Sunyaev-Zel'dovich tomography, *Phys. Rev. D* **100**, 083522 (2019).
- [26] S. C. Hotinli, G. P. Holder, M. C. Johnson, and M. Kamionkowski, Cosmology from the kinetic polarized Sunyaev Zel'dovich effect, [arXiv:2204.12503](https://arxiv.org/abs/2204.12503).
- [27] C. M. Hirata and U. Seljak, Intrinsic alignment-lensing interference as a contaminant of cosmic shear, *Phys. Rev. D* **70**, 063526 (2004).
- [28] M. Bartelmann and P. Schneider, Weak gravitational lensing, *Phys. Rep.* **340**, 291 (2001).
- [29] T. M. C. Abbott, M. Aguena, A. Alarcon, S. Allam, O. Alves *et al.* (DES Collaboration), Dark energy survey year 3 results: Cosmological constraints from galaxy clustering and weak lensing, *Phys. Rev. D* **105**, 023520 (2022).
- [30] D. Sarkar, P. Serra, A. Cooray, K. Ichiki, and D. Baumann, Cosmic shear from scalar-induced gravitational waves, *Phys. Rev. D* **77**, 103515 (2008).
- [31] M. Biagetti and G. Orlando, Primordial gravitational waves from galaxy intrinsic alignments, *J. Cosmol. Astropart. Phys.* **07** (2020) 005.
- [32] F. Schmidt and D. Jeong, Large-scale structure with gravitational waves. II. Shear, *Phys. Rev. D* **86**, 083513 (2012).
- [33] F. Schmidt, E. Pajer, and M. Zaldarriaga, Large-scale structure and gravitational waves. III. Tidal effects, *Phys. Rev. D* **89**, 083507 (2014).
- [34] Simons Observatory Collaboration, The Simons Observatory: Science goals and forecasts, *J. Cosmol. Astropart. Phys.* **02** (2019) 056.
- [35] K. Abazajian *et al.*, CMB-S4 decadal survey APC white paper, *Bull. Am. Astron. Soc.* **51**, 209 (2019).
- [36] LSST Science, LSST Project Collaboration, LSST Science Book, Version 2.0, [arXiv:0912.0201](https://arxiv.org/abs/0912.0201).
- [37] DESI Collaboration, The DESI experiment part I: Science, targeting, and survey design, [arXiv:1611.00036](https://arxiv.org/abs/1611.00036).
- [38] D. J. Schlegel *et al.*, Astro2020 APC white paper: The MegaMapper: a $z > 2$ spectroscopic instrument for the study of inflation and dark energy, [arXiv:1907.11171](https://arxiv.org/abs/1907.11171).
- [39] T. Hamana, M. Shirasaki, S. Miyazaki, C. Hikage, M. Oguri, S. More *et al.*, Cosmological constraints from cosmic shear two-point correlation functions with HSC survey first-year data, *Publ. Astron. Soc. Jpn.* **72**, 16 (2020).
- [40] A. L. Erickcek, S. M. Carroll, and M. Kamionkowski, Superhorizon perturbations and the cosmic microwave background, *Phys. Rev. D* **78**, 083012 (2008).
- [41] P. G. Castro, A. F. Heavens, and T. D. Kitching, Weak lensing analysis in three dimensions, *Phys. Rev. D* **72**, 023516 (2005).
- [42] D. J. Bacon, D. M. Goldberg, B. T. P. Rowe, and A. N. Taylor, Weak gravitational flexion, *Mon. Not. R. Astron. Soc.* **365**, 414 (2006).
- [43] P. Lemos, A. Challinor, and G. Efstathiou, The effect of Limber and flat-sky approximations on galaxy weak lensing, *J. Cosmol. Astropart. Phys.* **05** (2017) 014.
- [44] J. Blazek, M. McQuinn, and U. Seljak, Testing the tidal alignment model of galaxy intrinsic alignment, *J. Cosmol. Astropart. Phys.* **05** (2011) 010.
- [45] S. Ferraro, E. Schaan, and E. Pierpaoli, Is the Rees-Sciama effect detectable by the next generation of cosmological experiments?, [arXiv:2205.10332](https://arxiv.org/abs/2205.10332).
- [46] N. Sehgal *et al.*, CMB-HD: An ultra-deep, high-resolution millimeter-wave survey over half the sky, *Bull. Am. Astron. Soc.* **51**, 6 (2019).
- [47] M. Tegmark, A. N. Taylor, and A. F. Heavens, Karhunen-Loève eigenvalue problems in cosmology: How should we tackle large datasets?, *Astrophys. J.* **480**, 22 (1997).
- [48] BICEP/Keck Collaboration, The latest constraints on inflationary B-modes from the BICEP/Keck telescopes, in *Proceedings of the 56th Rencontres de Moriond on Cosmology* (2022), [arXiv:2203.16556](https://arxiv.org/abs/2203.16556).
- [49] M. S. Madhavacheril, N. Battaglia, K. M. Smith, and J. L. Sievers, Cosmology with the kinematic Sunyaev-Zel'dovich effect: Breaking the optical depth degeneracy with fast radio bursts, *Phys. Rev. D* **100**, 103532 (2019).
- [50] S. P. Boughn and R. G. Crittenden, A detection of the integrated Sachs-Wolfe effect, *New Astron. Rev.* **49**, 75 (2005).
- [51] F. X. Dupe, A. Rassat, J. L. Starck, and M. J. Fadili, Measuring the integrated Sachs-Wolfe effect, *Astron. Astrophys.* **534**, A51 (2011).
- [52] Planck Collaboration, Planck 2013 results. XIX. The integrated Sachs-Wolfe effect, *Astron. Astrophys.* **571**, A19 (2014).
- [53] D. Contreras, M. C. Johnson, and J. B. Mertens, Towards detection of relativistic effects in galaxy number counts using kSZ tomography, *J. Cosmol. Astropart. Phys.* **10** (2019) 024.
- [54] F. Schmidt and D. Jeong, Cosmic rulers, *Phys. Rev. D* **86**, 083527 (2012).